

Intra-cavity laser beam shaping

by

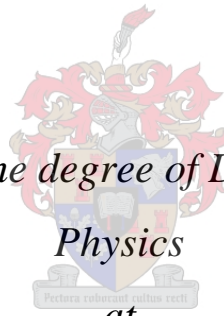
Igor A. Litvin

Thesis presented for the degree of Doctor of Philosophy in

Physics

at

Stellenbosch University



Physics Department

Promoter: Dr. Andrew Forbes

Co-Promoter: Prof Erich G Rohwer

Date: February 2010

Declaration

By submitting this thesis electronically, I declare that the entirety of the work contained therein is my own, original work, that I am the owner of the copyright thereof (unless to the extent explicitly otherwise stated) and that I have not previously in its entirety or in part submitted it for obtaining any qualification.

Date: 2 February 2010

A handwritten signature in blue ink, appearing to read 'L. van der ...', is positioned to the right of the date.

Abstract

There are many applications where a Gaussian laser beam is not ideal, for example, in areas such as medicine, data storage, science, manufacturing and so on, and yet in the vast majority of laser systems this is the fundamental output mode. Clearly this is a limitation, and is often overcome by adapting the application in mind to the available beam. A more desirable approach would be to create a laser beam as the output that is tailored for the application in mind – so called intra-cavity laser beam shaping. The main goal of intra-cavity beam shaping is the designing of laser cavities so that one can produce beams directly as the output of the cavity with the required phase and intensity distribution. Shaping the beam inside the cavity is more desirable than reshaping outside the cavity due to the introduction of additional external losses and adjustment problems. More elements are required outside the cavity which leads to additional costs and larger physical systems.

In this thesis we present new methods for phase and amplitude intra-cavity beam shaping. To illustrate the methods we give both an analytical and numerical analysis of different resonator systems which are able to produce customised phase and intensity distributions.

In the introduction of this thesis, a detailed overview of the key concepts of optical resonators is presented.

In Chapter 2 we consider the well-known integral iteration algorithm for intra-cavity field simulation, namely the Fox-Li algorithm and a new method (matrix method), which is based on the Fox-Li algorithm and can decrease the computation time of both the Fox-Li algorithm and any integral iteration algorithms. The method can be used for any class of integral iteration algorithms which has the same calculation integrals, with changing integrands. The given method appreciably decreases the computation time of these algorithms and approaches that of a single iteration.

In Chapter 3 a new approach to modeling the spatial intensity profile from Porro prism resonators is proposed based on rotating loss screens to mimic the apex losses of the prisms. A numerical model based on this approach is

presented which correctly predicts the output transverse field distribution found experimentally from such resonators.

In Chapter 4 we present a combination of both amplitude and phase shaping inside a cavity, namely the deployment of a suitable amplitude filter at the Fourier plane of a conventional resonator configuration with only spherical curvature optical elements, for the generation of Bessel–Gauss beams as the output.

In Chapter 5 we present the analytical and numerical analyses of two new resonator systems for generating flat–top–like beams. Both approaches lead to closed form expressions for the required cavity optics, but differ substantially in the design technique, with the first based on reverse propagation of a flattened Gaussian beam, and the second a metamorphosis of a Gaussian into a flat–top beam. We show that both have good convergence properties, and result in the desired stable mode.

In Chapter 6 we outline a resonator design that allows for the selection of a Gaussian mode by diffractive optical elements. This is made possible by the metamorphosis of a Gaussian beam into a flat–top beam during propagation from one end of the resonator to the other. By placing the gain medium at the flat–top beam end, it is possible to extract high energy in a low–loss cavity.

Samevatting

Daar is verskeie toepassings waar 'n Gaussiese laser bundel nie ideaal is nie, in gebiede soos mediese veld, stoor van data, vervaardiging en so meer, en tog word die meeste laser sisteme in die fundamentele mode bedryf. Dit is duidelik 'n beperking, en word meestal oorkom deur aanpassing van die toepassing tot die beskikbare bundel. 'n Beter benadering sou wees om 'n laser bundel te maak wat afgestem is op die toepassing - sogenaamde intra-resonator bundel vorming. Die hoofdoel van intra-resonator bundel vorming is om resonators te ontwerp wat direk as uitset kan lewer wat die gewenste fase en intensiteits-distribusie vertoon. Vorming van die bundel in die resonator is voordeliger omdat die vorming buite die resonator tot addisionele verliese asook verstellings probleme bydra. Meer elemente word benodig buite die resonator wat bydra tot hoër koste en groter sisteme.

In hierdie tesis word nuwe fase en amplitude intra-resonator bundelvormings metodes voorgestel. Om hierdie metode te demonstree word analitiese en numeriese analyses vir verskillende resonator sisteme wat aangepaste fase en intensiteit distribusies produseer, bespreek.

In die inleiding van die tesis word 'n detailleer oorsig oor die sleutel konsepte van optiese resonators voorgelê.

In hoofstuk 2 word die bekende integraal iterasie algoritme vir intra-resonator veld simulatie, naamlik die Fox-Li algoritme, en 'n nuwe metode (matriks metode), wat gebaseer is op die Fox-Li algoritme, en die berekeningstyd van beide die Fox-Li algoritme en enige ander integraal iterasie algoritme verminder. Die metode kan gebruik word om enige klas van integraal iterasie algoritmes wat dieselfde berekenings integrale het, met veranderde integrante (waar die integrand die veld van die lig golf is in die geval van die Fox-Li algoritme, IFTA, en die skerm metode. Die voorgestelde metode verminder die berekeningstyd aansienlik, en is benaderd die van 'n enkel iterasie berekening.

In hoofstuk 3 word 'n nuwe benadering om die modellering van die ruimtelike intensiteitsprofiel van Porro prisma resonators, gebaseer op roterende verliese skerms om die apeks-verliese van die prisma's te benader, voorgestel. 'n

Numeriese model gebaseer op hierdie benadering wat die uitset van die transversale veld distribusie in eksperimentele resonators korrek voorspel, word voorgestel.

In hoofstuk 4 word 'n tegniek vir die generering van Bessel-Gauss bundels deur die gebruik van 'n kombinasie van amplitude en fase vorming in die resonator en 'n geskikte amplitude filter in die Fourier vlak van 'n konvensionele resonator konfigurasie met optiese elemente wat slegs sferiese krommings het, voorgestel.

In hoofstuk 5 word die analitiese en numeriese analyses van twee nuwe resonator sisteme vir die generering van sogenaamde "flat-top" bundels voorgestel. Beide benaderings lei na 'n geslote vorm uitdrukking vir die resonator optika wat benodig word, maar verskil noemenswaardig in die ontwerp-tegniek. Die eerste is baseer op die terug voortplanting van plat Gaussiese bundel, en die tweede op metamorfose van Gaussiese "flat-top" bundel. Ons toon aan dat beide tegnieke goeie konvergensie het, en in die gevraagde stabiele modus lewer.

In hoofstuk 6 skets ons die resonator ontwerp wat die selektering van 'n Gaussiese modus deur diffraktiewe optiese element moontlik maak. Dit word moontlik deur die metamorfose van 'n Gaussiese bundel na 'n "flat-top" gedurende die voortplanting van die een kant van die resonator na die ander. Deur die wins medium aan die "flat-top" kant van die bundel te plaas word dit moontlik om hoë energie te onttrek in 'n lae verlies resonator.

Acknowledgements

I would like to thank my supervisors Dr. Andrew Forbes and Prof. Erich G Rohwer for their help with this thesis and their useful discussions and advice. Thank you to my past supervisors, Dr. A. M. Belsky and Dr. N. A. Khilo, for their help with the development of my research skills in theoretical optics. Also thank you to Mr Dieter Preussler and Mr Daniel Esser for their useful discussions and advice with the experimental part of this thesis. I am grateful to my mother N. S. Litvin for believing in me and for her financial and emotional support. I am thankful to my wife M. I. Litvin and my friends for creating a goal for my work and supporting me with a good work environment.

Table of Contents

| | |
|---|-----|
| Declaration..... | i |
| Abstract | ii |
| Samevatting..... | iv |
| Acknowledgement | vi |
| Table of Contents..... | vii |
| List of Figures | x |
| List of author publications and patents including in the thesis | xiv |

1. Introduction

| | |
|--|----|
| 1.1 Electromagnetic boundary conditions | 1 |
| 1.1.1 Boundary conditions for the electric field | 2 |
| 1.1.2 Normal component of \mathbf{D} | 3 |
| 1.1.3 Tangential component of \mathbf{E} | 4 |
| 1.1.4 Dielectric – Perfect Conductor | 5 |
| 1.2 Modes of rectangular closed cavity | 6 |
| 1.3 Modes of open cavity..... | 12 |
| 1.4 Stability of open cavity..... | 14 |
| 1.5 Fresnel number of open cavity | 17 |

2. Fox–Li mode development analysis and a matrix method

| | |
|---------------------------|----|
| 2.1 Fox–Li algorithm..... | 19 |
|---------------------------|----|

| | |
|--|----|
| 2.2 Matrix method | 20 |
| 2.3 Other applications | 23 |
| 2.3.1 Iterative Fourier transform algorithm | 23 |
| 2.3.2 The simulation of turbulence transformation of the optical field | 25 |
| 2.4 Conclusion | 26 |
| 3. Petal-like modes in Porro prism resonator | |
| 3.1 Introduction..... | 27 |
| 3.2 Porro resonator concept | 29 |
| 3.3 Test resonator..... | 36 |
| 3.3.1 Experimental set-up | 37 |
| 3.3.2 Numerical modelling | 37 |
| 3.4 Result and discussion..... | 38 |
| 3.5 Conclusion | 41 |
| Appendix (Double pulse)..... | 41 |
| 4. Bessel – Gauss resonator with internal amplitude filter | |
| 4.1 Introduction..... | 43 |
| 4.2 Bessel–Gauss resonator concept..... | 45 |
| 4.2.1 Bessel–Gauss beams | 45 |
| 4.2.2 Fourier transforming resonator | 46 |
| 4.2.3 Resonator modes..... | 48 |
| 4.3 Fourier optics analysis | 51 |
| 4.4 Fox–Li analysis..... | 54 |
| 4.5 Conclusion | 56 |
| 5. Intra-cavity flat-top beam generation | |
| 5.1 Introduction..... | 57 |
| 5.2 Reverse propagation technique..... | 60 |
| 5.3 Flattened Gaussian beam resonator | 62 |
| 5.3.1 Flattened Gaussian beams..... | 62 |

| | |
|---|----|
| 5.3.2 Simulation results | 64 |
| 5.4 Flat-top resonator | 66 |
| 5.4.1 Theory | 66 |
| 5.4.2 Simulation results | 68 |
| 5.5 Discussion | 69 |
| 5.6 Conclusion | 72 |
| 6. Gaussian mode selection with intra-cavity diffractive optics | |
| 6.1 Introduction | 73 |
| 6.2 Gaussian mode selection | 75 |
| 6.3 Numerical analysis and discussion | 77 |
| 6.4 Conclusion | 79 |
| Conclusion | 81 |
| References | 84 |

List of Figures

Fig. 1.1. The changing electric field on a boundary between two different media.

Fig. 1.2. Gauss's flux law for the derivation of the normal components of the electric field on the boundary.

Fig. 1.3. Faraday's law for the derivation of the tangential components of the electric field on the boundary.

Fig. 1.4. The behavior of electric and magnetic fields on the boundary of a dielectric - perfect conductor.

Fig. 1.5. The open resonator consisting of two parallel plane discs.

Fig. 1.6. The representation of an open cavity by waveguides consisting of a set of thin lenses.

Fig. 1.7. The angles of the light ray before and after passing through the thin lens.

Fig. 1.8. The stability region of an open cavity.

Fig. 1.9. Young's representation of the diffraction on a round screen.

Fig. 2.1. The illustration of Fox Li method.

Fig. 2.2. Illustration to matrix method development.

Fig. 3.1. A typical Porro prism based Nd:YAG laser with passive Q-switch, showing the following optical elements: Porro prisms (elements a and h); intra-cavity lenses (elements b and g); a beamsplitter cube (element c); a quarter wave plate (element d), and a passive Q-switch (element e).

Fig. 3.2. Illustration of the effect of phase and intensity screens on an incident field.

Fig. 3.3. (a) – (e): Evolution of a ray as it is reflected back and forth in the resonator, for starting Porro angle $\alpha = 60^\circ$. After 3 round trips the pattern is complete (e) and starts to repeat. (f) – (j): Equivalent case but with $\alpha = 30^\circ$, and now taking 6 round trips for completion.

Fig. 3.4. The apexes of two Porro prisms at angles ϕ_1 and ϕ_2 . Initially the apex of PP 1 is in the horizontal plane (a), but after successive reflections about the inverting edges of the two prisms the apex will appear to be rotating about the circle: (b) 1 pass, (c) 2 passes and (d) 3 passes.

Fig. 3.5. Plot of the discrete set of angles α that give rise to a petal pattern, with the corresponding number of petals to be observed. Data calculated for $m \in [1,100]$ and $i \in [1,50]$.

Fig. 3.6. Photograph of assembled laser. The beamsplitter cube and one of the Porro prisms can be made out on the left of the assembly.

Fig. 3.7. The analytical model depiction of finitely sub-divided fields in (a) and (b), and an infinitely sub-divided field in (c). Numerically this results in a pattern with (d) 10 petals, (e) 14 petals and (f) no petals. The corresponding experimentally observed output is shown in (g) – (i).

Fig. 3.8. Analytically calculated sub-division of the field using Eqs. (3.4) and (3.7) (top row), with corresponding petal patterns calculated numerically using this model.

Fig. 3.9. Plot of the round-trip loss as a function of the number of petals as predicted by the numerical model.

Fig. 3.10. The transverse field distribution, with (a) two and (b) one pulse. The angle between the Porro prisms is 13 degrees (giving 14 spots).

Fig. 4.1. Illustration of the Bessel-Gauss resonator. Mirror M1 is obscured by a disk of radius d , thereby forming an annular lossless zone in the region $a < r < b$. Each mirror has a radius of curvature of $2f$ and they are separated by a distance of $2f$.

Fig. 4.2. The BGB is formed in the shaded region of the resonator, and changes in intensity as it propagates through this volume. Five intensity plots are shown corresponding to planes (a) through (e) within the resonator for the zeroth Bessel mode ($n=0$). The starting mode was calculated using the Fox-Li algorithm with ten round trips, Fresnel number $N = 6$ and $a = \frac{5}{6}b$, and then propagated using Eq. (4.6).

Fig. 4.3. Mirror phase as calculated from Eq. (4.7) (solid curve) as compared to the numerically calculated phase using the Fox-Li algorithm (data points).

Fig. 4.4. The dependence of diffraction losses on radius b for the various orders of BGBs (even modes as solid curve, odd modes as dashed curve): (a) shows a general trend for the zeroth and first order mode of decreasing oscillation strength with increasing mirror radius due to the Gaussian envelope dominance when $b \gg w_2$. In this plot $a = 0.9b$, and thus the losses increase with b . A zoomed in area (between the vertical solid lines) is shown in (b), with the out of

phase oscillations of the odd and even modes evident; (c) shows plot (a) but with a fixed in value.

Fig. 4.5. The diffraction losses, as calculated by the Fourier approach, showing the zeroth order mode (0) with higher losses than some odd order modes (shown starting at 1, dashed curve). Calculations done at $b = 1.465$ mm corresponding to cross-section A of Fig. 4.4 (b).

Fig. 4.6. The zero order mode (0) now has the lowest losses, with a clear out-of-phase oscillation in the loss for odd (starting at 1, dashed curve) and even (starting at 0, solid curve) modes. Calculations done at $b = 1.50$ mm corresponding to cross-section B of Fig. 4(b).

Fig. 4.7. The dependence of the diffraction losses per round trip on the mode number, as calculated using the Fox-Li method. Odd modes are shown starting at 1 in the dashed curve, while even modes are shown starting at 0 in the solid curve. The results are in very good agreement with those shown in Fig. 4.6.

Fig. 4.8. Examples of the calculated BGBs with their corresponding Fourier transforms: (a) J_1 , (b) J_5 and (c) J_6 Bessel orders.

Fig. 5.1. A schematic of the resonator to be modeled: with output coupling at M_2 . Mirrors M_1 and M_2 can either be considered as elements with non-spherical curvature, or as depicted above, as flat mirrors with an appropriate transmission DOE placed immediately in front of each.

Fig. 5.2. Calculated phase profile required for the DOE at mirror M_1 . The requirement for the DOE at M_2 is that it is a planar surface.

Fig. 5.3. The simulated field at mirror M_1 (red) and M_2 (blue): (a) intensity, showing a near perfect flat-top beam at M_2 , with slight change in flatness after propagating across the resonator to M_1 , (b) phase of the field, with a flat wavefront at M_2 as anticipated from the design.

Fig. 5.4. The simulated field as it propagates across the resonator after stabilization, from M_1 (left) to M_2 (right). The perfect flat-top beam develops some intensity 'structure' as it propagates away from M_2 . This is in accordance with the propagation properties of such fields, and may be minimized by suitable choice of Rayleigh range of the field.

Fig. 5. The calculated required phases of the two DOEs, DOE₁ in blue and DOE₂ in red, to achieve the flat-top output mode.

Fig. 5.6. The simulated field at mirror M_1 (red) and M_2 (blue): (a) intensity, showing a near perfect flat-top beam at M_2 , changing into a perfect Gaussian after propagating across the resonator to M_1 , (b) phase of the field, with a flat wavefront at M_1 as anticipated from the design.

Fig. 5.7. The simulated field as it propagates across the resonator after stabilization, from M_1 (left) to M_2 (right). The perfect Gaussian beam (a) gradually changes into a perfect flat-top beam (e) on one pass through the resonator. In this design the field also decreases in size, as noted from the size of the grey scale images.

Fig. 5.8. The simulated losses as a starting field of random noise is propagated through the resonator, shown as a function of the number of round trips taken, for: (a) resonator A and (b) resonator B . The losses stabilize in both resonators, and both show a characteristic oscillation in the losses as the field converges to the stable mode of lowest loss.

Fig. 6.1: Schematic of the resonator concept.

Fig. 6.2: Numerical results of the Fox-Li analysis, showing (a) Gaussian and flat-top beams after starting from random noise, and (b) calculated phase profile of each DOE, with the analytical phase function for the second DOE shown as data points.

Fig. 6.3: Cross-sections of the first three higher-order competing modes, shown at mirror M_2 .

List of author's publications and patents included in the thesis

Patents

Igor A. Litvin and Andrew Forbes, "Laser Beam Generation", P45999ZP00, RSA provisional patent.

Book Chapters

Philip W. Loveday, Igor A. Litvin, Craig S. Long, Andrew Forbes, "Preliminary results on dynamic intra-cavity laser mode selection," in press.

Peer reviewed Journal Papers

1. Igor A. Litvin, Liesl Burger, Andrew Forbes, "Petal-like modes in Porro prism resonators," *Opt. Express*, 15 (21), 14065-14077, 2007.
2. Igor A. Litvin and Andrew Forbes, "Bessel-Gauss Resonator with Internal Amplitude Filter," *Opt. Commun.*, 281 (9), 2385-2392, 2008.
3. Igor A. Litvin, Melanie G. McLaren, Andrew Forbes, "A conical wave approach to calculating Bessel-Gauss beam reconstruction after complex obstacles," *Opt. Commun.*, 282 (6), 1078-1082, 2008.
4. Igor A. Litvin and Andrew Forbes, "Gaussian mode selection with intra-cavity diffractive optics," *Opt. Lett.*, 34 (19), 2991-2993, 2009.
5. Igor A. Litvin and Andrew Forbes, "Intra-cavity flat-top beam generation," *Opt. Express*, 17 (18), 15891-15903, 2009.
6. Igor A. Litvin, N. Khilo, A. Forbes, V. Belyi, "Intra-cavity generation of longitudinally dependant Bessel like beams," accepted for publication in *Opt. Express*, 2010.

International Conference Papers

1. Igor A. Litvin, Liesl Burger, Andrew Forbes, “Analysis of transverse field distribution in Porro prism resonator,” *Proc. of SPIE*, 6346, 63462G, 2007.
2. Igor A. Litvin and Andrew Forbes, “Impact of phase errors at the conjugate step on the propagation of intensity and phase shaped laser beams,” *Proc. of SPIE*, 6663, 666303, 2007.
3. Igor. A. Litvin, L. Burger, M. P. De Gama, A. Mathye, A. Forbes, “Laser beam shaping limitations for laboratory simulation of turbulence using a phase-only spatial light modulator,” *Proc. of SPIE*, 6663, 66630R, 2007.
4. Igor A. Litvin, Philip W. Loveday, Craig S. Long, Nikolai S. Kazak, Vladimir Belyi, Andrew Forbes, “Intra-cavity mode competition between classes of flat-top beams,” *Proc. of SPIE*, 7062, 706210, 2008.
5. Andrew Forbes, Craig S. Long, Igor A. Litvin, Philip W. Loveday, Vladimir Belyi, Nikolai S. Kazak, “Variable flattened Gaussian beam order selection by dynamic control of an intra-cavity diffractive mirror,” *Proc. of SPIE*, 7062, 706219, 2008.
6. Igor A. Litvin, Melanie G. McLaren, Andrew Forbes, “Propagation of obstructed Bessel and Bessel-Gauss beams,” *Proc. of SPIE*, 7062, 706218, 2008.
7. Igor A. Litvin and Andrew Forbes, “Intra-cavity flat-top beam generation,” *Proc. of SPIE*, 7430, 74300M, 2009.
8. Igor A. Litvin, N. Khilo, Andrew Forbes, V. Belyi, “Intra-cavity generation of longitudinal dependant Bessel like beams,” *Proc. of SPIE*, 7430, 743010, 2009.

Chapter 1

Introduction

In this Section, a detailed overview of the key concepts of optical resonators is presented. We have tried to begin from the basics of resonator theory, namely electromagnetic boundary conditions which correspond to most characteristic electromagnetic field behaviors inside the cavity. Actually, the interaction of the electromagnetic field with a conductive surface is a source of characteristic for cavity states of the electromagnetic field which has a different property in comparison with free space fields, namely the possibility of a wave oscillating with exclusively discrete values of wave vectors and furthermore electromagnetic field amplitudes in a cavity (modes or characteristic oscillations of the cavity). It is one of the prominent features extensively used for producing monochromatic beams having a small divergence. To decrease the number of characteristic oscillations inside the cavity and consequently raise the monochromatic property and decrease the divergence of the output, the open cavity was proposed.

For the convenience of the reader, we present detailed derivations and definitions of some useful parameters which are universally used and are able to give relatively good representation of the behavior of the electromagnetic wave inside the cavity, namely the Fresnel number and cavity stability.

1.1 Electromagnetic boundary conditions

We assume that the reader has previously encountered Maxwell's equations, at least briefly, and understands that they provide the most fundamental description of electric and magnetic fields. For a review of this field the reader is referred to standard texts on the subject [1.1]. The integral forms of Maxwell's equations describe the behavior of electromagnetic field quantities in all geometric configurations. The differential forms of Maxwell's equations are

only valid in regions where the parameters of the media are constant or vary smoothly i.e. in regions where $\varepsilon(x, y, z, t)$, $\mu(x, y, z, t)$ and $\sigma(x, y, z, t)$ (dielectric constant, magnetic permeability and conductivity of the medium respectively) do not change abruptly. In order for a differential form to exist, the partial derivatives must exist, and this requirement breaks down at the boundaries between different materials. For the special case of points along boundaries, we must derive the relationship between field quantities immediately on either side of the boundary from the integral forms (as was done for the differential forms under differentiable conditions). Later, we shall apply these boundary conditions to examine the behavior of EM waves at interfaces between different materials.

1.1.1 Boundary conditions for the electric field

Consider how the electric field \mathbf{E} may change on either side of a boundary between two different media, as illustrated in Fig.1.1.

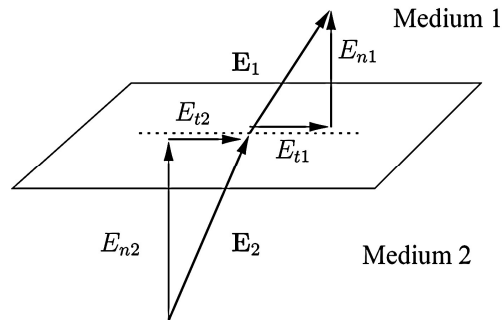


Fig. 1.1. The changing electric field at the boundary between two different media.

The vector \mathbf{E}_1 refers to the electric field in medium 1, and \mathbf{E}_2 in medium 2. One can further decompose vectors \mathbf{E}_1 and \mathbf{E}_2 into normal (perpendicular to the interface) and tangential (in the plane of the interface) components. These components labeled E_{n1} , E_{t1} and E_{n2} , E_{t2} lie in the plane of vectors \mathbf{E}_1 and \mathbf{E}_2 . To derive the boundary conditions for \mathbf{E} , we must examine two of Maxwell's equations:

$$\oint \vec{E} \cdot d\vec{l} = -\int_s \frac{\partial \vec{B}}{\partial t} \cdot d\vec{S} \quad (1.1)$$

and

$$\oint \vec{D} \cdot d\vec{S} = \int_v \rho dV, \quad (1.2)$$

which will allow us to relate the tangential and normal components of \mathbf{E} on either side of the boundary.

1.1.2 Normal component of \mathbf{D}

The boundary condition for the normal component of the electric field can be obtained by applying Gauss's flux law

$$\oint \vec{D} \cdot d\vec{S} = \int_V \rho dV \quad (1.3)$$

to a small 'pill-box', positioned such that the boundary sits between its 'upper' and 'lower' surfaces as shown in the illustration (see Fig.1.2).

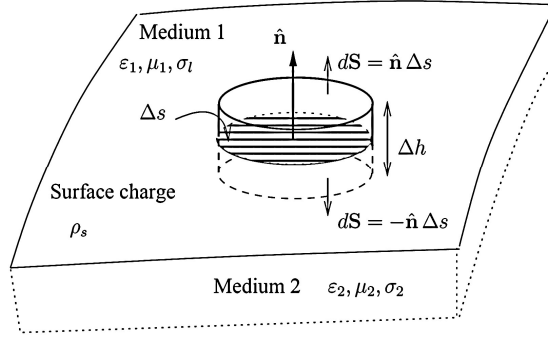


Fig. 1.2. Gauss's flux law for the derivation of the normal components of the electric field on the boundary.

If we shrink the length of side wall Δh to zero, but in such a way that all of the electric flux enters or leaves the pill-box through the top and bottom surfaces, then

$$\oint \vec{D} \cdot d\vec{S} \rightarrow \vec{D}_1 \cdot \vec{n} \Delta S + \vec{D}_2 \cdot (-\vec{n}) \Delta S = D_{n1} \Delta S - D_{n2} \Delta S, \quad (1.4)$$

where D_{n1} and D_{n2} are the normal components of the flux density vector immediately on either side of the boundary in mediums 1 and 2, and ΔS is the elemental surface area.

The amount of charge enclosed as $\Delta h \rightarrow 0$ depends on whether there exists a layer of charge on the surface (i.e. an infinitesimally thin layer of charge). If a surface charge layer exists then

$$\int_V \rho dV = \rho_s \Delta S, \quad (1.5)$$

and thus

$$D_{n1} \Delta S - D_{n2} \Delta S = \rho_s \Delta S. \quad (1.6)$$

From which we conclude

$$D_{n1} - D_{n2} = \rho_s. \quad (1.7)$$

For the case where $\rho_s = 0$,

$$D_{n1} = D_{n2}; \quad (1.8)$$

or in terms of the electric field E ,

$$\epsilon_1 E_{n1} = \epsilon_2 E_{n2}. \quad (1.9)$$

1.1.3 Tangential component of E

We can derive the tangential component of E by applying Faraday's law to a small rectangular loop positioned in across the boundary, and in the plane of E_1 and E_2 , as illustrated in the diagram below (see Fig .1.3).

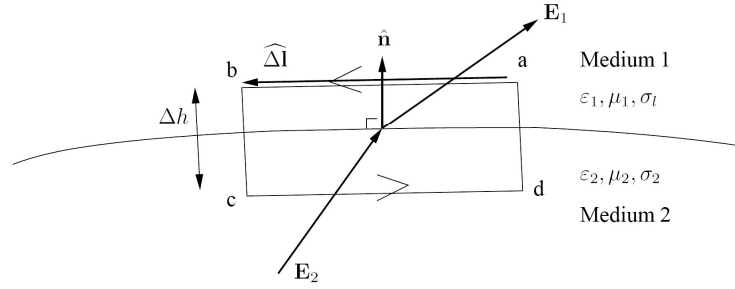


Fig. 1.3. Faraday's law for the derivation of the tangential components of the electric field on the boundary.

Consider the limiting case where the sides perpendicular to the boundary are allowed shrink to zero. In the limit as $\Delta h \rightarrow 0$, the magnetic flux threading the loop shrinks to zero, and thus

$$\oint \vec{E} \cdot d\vec{l} \rightarrow \int_a^b \vec{E} \cdot d\vec{l} + \int_c^d \vec{E}_2 \cdot d\vec{l} = 0 \Rightarrow \vec{E}_1 \cdot \Delta\vec{l} + \vec{E}_2 \cdot (-\Delta\vec{l}) = 0. \quad (1.10)$$

Writing the tangential components of E_1 and E_2 along the contour as E_{t1} and E_{t2} , we have

$$E_{t1}\Delta l - E_{t2}\Delta l = 0. \quad (1.11)$$

From which we conclude that on either side of the boundary,

$$E_{t1} - E_{t2} = 0 \quad (1.12)$$

i.e. the tangential components immediately on either side of a boundary are equal.

1.1.4 Dielectric – Perfect Conductor

If one of the media is dielectric (say medium 1 is air), and the other medium (medium 2) is a perfect conductor $\sigma_2 \rightarrow \infty$, then $E_{n2} = 0$ and $E_{t2} = 0$ inside the perfect conductor.

Since $D_{n1} - D_{n2} = \rho_s$, we conclude that $D_{n1} = \rho_s$

Since $E_{t1} = E_{t2}$ and $E_{t2} = 0$, we conclude that $E_{t1} = 0$, i.e. there exists no tangential component in the dielectric.

In vector form we state the boundary conditions for the field in the dielectric as

$$\vec{D}_1 \cdot \vec{n} = \rho_s \quad (1.13)$$

and

$$\vec{n} \times \vec{D} = 0 \quad (1.14)$$

The E field lines always meet a perfect conductor perpendicular to the surface, and magnetic field lines parallel to the surface as is illustrated in the figure below (see Fig.1.4):

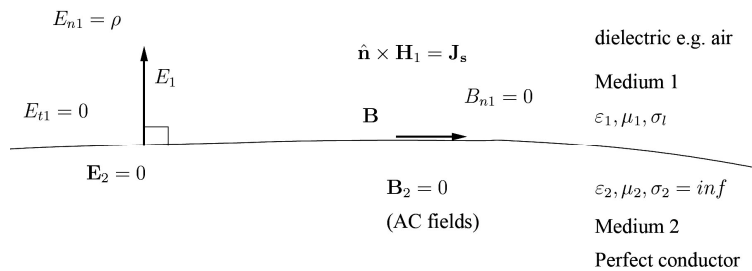


Fig. 1.4. The behavior of electric and magnetic fields on the boundary of a dielectric - perfect conductor.

For AC fields, no magnetic field exists in a perfect conductor - why? Recall that $\nabla \times \vec{E} = -\partial \vec{B} / \partial t$ and since $E = 0$ in a perfect conductor, $\nabla \times \vec{E} = 0$ and hence $\partial \vec{B} / \partial t = 0$. In other words, no changing magnetic field can exist in a perfect conductor, and hence $B_{n2} = B_{n1} = 0$. A surface current can still exist, implying a tangential component of \vec{B}_1 can exist. These two conditions can be expressed in vector form as

$$\vec{B}_1 \cdot \vec{n} = 0, \quad (1.15)$$

$$\vec{n} \times \vec{H}_1 = \vec{J}_s. \quad (1.16)$$

These boundary conditions are useful for establishing, for example, the charge density or current distribution on the surface of a conductor, when the field in the dielectric is known or specified.

These boundary conditions will be applied when analyzing the reflection of an electromagnetic plane wave off the surface of a perfect conductor.

1.2 Modes of rectangular closed cavity

We will outline the property of the electromagnetic field in a rectangular closed cavity using the approach of Ref [1.2]. For a neutral dielectric medium (one with no free charges) Maxwell's equations are

$$\vec{\nabla} \cdot \vec{D} = 0, \quad (1.17)$$

$$\vec{\nabla} \cdot \vec{B} = 0, \quad (1.18)$$

$$\vec{\nabla} \times \vec{E} = -\partial \vec{B} / \partial t, \quad (1.19)$$

$$\vec{\nabla} \times \vec{H} = \partial \vec{D} / \partial t, \quad (1.20)$$

We will be interested only in nonmagnetic media, for which

$$\vec{B} = \mu_0 \vec{H} \quad (1.21)$$

where $\mu_0 = 4\pi \times 10^{-7} \text{ N/A}^2$ and the electric displacement \vec{D} is defined as

$$\vec{D} = \epsilon_0 \vec{E} + \vec{P} \quad (1.22)$$

where $1/4\pi\epsilon_0 = 9.9874 \times 10^9 \text{ Nm}^2/\text{C}^2$ and the polarization \vec{P} is the electric dipole moment per unit volume of the medium. \vec{P} is the only term in Maxwell equations relating directly to the medium.

Applying the curl operation to both sides of Eq. (1.23), we obtain

$$\vec{\nabla} \times (\vec{\nabla} \times \vec{E}) = -\vec{\nabla} \times \partial \vec{B} / \partial t = -\partial / \partial t (\vec{\nabla} \times \vec{B}). \quad (1.23)$$

Now we use the general identity

$$\vec{\nabla} \times (\vec{\nabla} \times \vec{E}) = \vec{\nabla} (\vec{\nabla} \cdot \vec{E}) - \vec{\nabla}^2 \vec{E} \quad (1.24)$$

of vector calculus. Together with Eq. (1.21) and Maxwell's Eq. (1.20), to write

$$\vec{\nabla} (\vec{\nabla} \cdot \vec{E}) - \vec{\nabla}^2 \vec{E} = -\mu_0 \partial^2 \vec{D} / \partial t^2. \quad (1.25)$$

Finally we use the definition (1.22) of \vec{D} and rearrange the terms

$$\vec{\nabla}(\vec{\nabla} \cdot \vec{E}) - \nabla^2 \vec{E} - \frac{1}{c^2} \frac{\partial^2 \vec{E}}{\partial t^2} = \frac{1}{\epsilon_0 c^2} \frac{\partial^2 \vec{P}}{\partial t^2}. \quad (1.26)$$

Here we have used the fact that

$$\epsilon_0 \mu_0 = 1/c^2, \quad (1.27)$$

where $c = 2.998 \times 10^8 \text{ ms}^{-1}$ is the velocity of light in a vacuum.

Eq. (1.26) is a partial differential equation with independent variables x , y , z , and t in Cartesian coordinates. It tells us how the electric field depends on the electric dipole moment density \vec{P} of the medium. We will be particularly interested in *transverse* fields (sometimes called *solenoid* or *radiation* fields). Such fields satisfy

$$\vec{\nabla} \cdot \vec{E} = 0. \quad (1.28)$$

Transverse fields therefore satisfy the inhomogeneous wave equation

$$\nabla^2 \vec{E} - \frac{1}{c^2} \frac{\partial^2 \vec{E}}{\partial t^2} = \frac{1}{\epsilon_0 c^2} \frac{\partial^2 \vec{P}}{\partial t^2}. \quad (1.29)$$

This is the fundamental electromagnetic field equation for our purpose. In order to make any use of it we must somehow specify the polarization \vec{P} . This cannot be done solely within the framework of the Maxwell equations, for \vec{P} is a property of the material medium in which the field \vec{E} propagates.

However, we will finish this Section with a discussion of the solution to the homogeneous (free-space) wave equation, which applies when there is no polarization present. In general, the laser resonator theory is based on the free-space wave equation and free-space solution. Such solutions are useful; even though lasers do not operate in a vacuum, because most laser media are optically homogeneous. In a homogeneous linear and isotropic dielectric medium, the polarization is aligned with and proportional to the electric field $\vec{E} = \alpha \vec{P}$. In this case Eq. (1.29) will have an equivalent form to the wave equation in free space (see Eq. (1.30)) but with different constant before second time derivative namely $1/c^2 \rightarrow \alpha/c^2$.

We will consider only the case of a rectangular cavity. We also assume we have perfectly reflecting walls; then the components of the electric field parallel to the walls must vanish on the walls. The electric field inside the cavity satisfies the wave equation

$$\vec{\nabla}^2 \vec{E} - \frac{1}{c^2} \frac{\partial^2 \vec{E}}{\partial t^2} = 0. \quad (1.30)$$

For a monochromatic field of angular frequency $\omega = 2\pi\nu$, we use the complex-field representation (where the electric field is understood to be the real part of the right-hand side):

$$\vec{E}(\vec{r}, t) = \vec{E}_0(\vec{r}) \exp(-i\omega t) \quad (1.31)$$

and Eq. (1.30) becomes

$$\nabla^2 \vec{E}_0(\vec{r}) + k^2 \vec{E}_0(\vec{r}) = 0, \quad k \equiv \omega/c. \quad (1.32)$$

That is,

$$(\nabla^2 + k^2) E_{0x}(\vec{r}) = 0 \quad (1.33)$$

and likewise for the y and z components.

To solve Eq. (1.33), it is convenient to use the method of separation of variables, written as:

$$E_{0x}(x, y, z) = F(x)G(y)H(z) \quad (1.34)$$

and then substitute into Eq. (1.33). After carrying out the differentiations required by $\nabla^2 = \partial^2/\partial x^2 + \partial^2/\partial y^2 + \partial^2/\partial z^2$, we divide through by the product FGH and obtain

$$\frac{1}{F} \frac{\partial^2 F}{\partial x^2} + \frac{1}{G} \frac{\partial^2 G}{\partial y^2} + \frac{1}{H} \frac{\partial^2 H}{\partial z^2} + k^2 = 0. \quad (1.35)$$

Since each of the first three terms on the left side is a function of a different independent variable, Eq. (1.35) can only be true for all x , y , and z if each term is separately constant, i.e.,

$$\frac{1}{F} \frac{d^2 F}{dx^2} = -k_x^2, \quad (1.36a)$$

$$\frac{1}{G} \frac{d^2 G}{dy^2} = -k_y^2, \quad (1.36b)$$

$$\frac{1}{H} \frac{d^2 H}{dz^2} = -k_z^2, \quad (1.36c)$$

with

$$k_x^2 + k_y^2 + k_z^2 = k^2. \quad (1.37)$$

The boundary condition that the tangential component of the electric field vanishes on the cavity walls means that

$$E_{0x}(x, y = 0, z) = E_{0x}(x, y = L_y, z) = 0, \quad (1.38a)$$

$$E_{0x}(x, y, z = 0) = E_{0x}(x, y, z = L_z) = 0 \quad (1.38b)$$

or

$$G(0) = G(L_y) = 0, \quad (1.39a)$$

$$H(0) = H(L_z) = 0. \quad (1.39b)$$

A solution of Eq. (1.36b) satisfying the boundary condition $G(0) = 0$ is

$$G(y) = \sin(k_y y). \quad (1.40)$$

In order to satisfy $G(L_y) = 0$ as well, we must have $\sin(k_y L_y) = 0$, or in other words

$$k_y L_y = m\pi, m=0, 1, 2, \dots \quad (1.41a)$$

In exactly the same way we find that solutions of Eq. (1.36c) satisfy Eq. (1.39b) are only possible if

$$k_z L_z = n\pi, n=0, 1, 2, \dots \quad (1.41b)$$

Finally, consideration of the equation for the y and z components of $\vec{E}_0(\vec{r})$, together with the appropriate boundary conditions, shows that allowed solutions for $\vec{E}_0(\vec{r})$ must satisfy Eqs. (1.41a), (1.41b) and

$$k_x L_x = l\pi, l=0, 1, 2, \dots \quad (1.41c)$$

The solution for the components of $\vec{E}(\vec{r}, t)$ satisfying Maxwell's equations and the boundary conditions inside the cavity are

$$E_x(x, y, z, t) = A_x \exp(-i\omega t) \cos\left(\frac{l\pi x}{L_x}\right) \sin\left(\frac{m\pi y}{L_y}\right) \sin\left(\frac{n\pi z}{L_z}\right), \quad (1.42a)$$

$$E_y(x, y, z, t) = A_y \exp(-i\omega t) \sin\left(\frac{l\pi x}{L_x}\right) \cos\left(\frac{m\pi y}{L_y}\right) \sin\left(\frac{n\pi z}{L_z}\right), \quad (1.42b)$$

$$E_z(x, y, z, t) = A_z \exp(-i\omega t) \sin\left(\frac{l\pi x}{L_x}\right) \sin\left(\frac{m\pi y}{L_y}\right) \cos\left(\frac{n\pi z}{L_z}\right). \quad (1.42c)$$

Where the coefficients A_x , A_y and A_z must satisfy the condition

$$\frac{l}{L_x} A_x + \frac{m}{L_y} A_y + \frac{n}{L_z} A_z = 0, \quad (1.43)$$

implied by the Maxwell equation $\vec{\nabla} \cdot \vec{E} = 0$, valid in the empty cavity.

From Eqs. (1.37) and (1.41) we have

$$k^2 = \pi^2 \left(\frac{l^2}{L_x^2} + \frac{m^2}{L_y^2} + \frac{n^2}{L_z^2} \right). \quad (1.44)$$

The possible modes of the rectangular closed cavity have allowed frequencies determined by Eq. (1.44) and $k = \omega/c = 2\pi\nu/c$:

$$\nu = \nu_{lmn} = \frac{c}{2} \left(\frac{l^2}{L_x^2} + \frac{m^2}{L_y^2} + \frac{n^2}{L_z^2} \right)^{1/2}. \quad (1.45)$$

The number of modes available in a cavity is infinite. This is clear because in Eq. (1.45), for example, an infinite number of values are permitted for any of the three mode indices l , m and n . However, the number of modes whose frequency lies in the neighborhood $d\nu$ of a given value ν is finite. This number is related to the number of modes whose frequency is less than ν , and it is this number we will determine first.

The number of modes we want is the number of terms in the triple sum:

$$N = \sum_l \sum_m \sum_n, \quad (1.46)$$

where the upper limits on the sums are determined by the maximum frequency to be included. The simplest approach to this problem is to stipulate that the cavity length is much larger than a typical wavelength and consequently the mode spacing is negligible (obviously true for realistic cavities and optical wavelengths). Then the discrete nature of the sum is not important and we can rewrite the sum as a triple integral:

$$N = \int dl \int dm \int dn. \quad (1.47)$$

In addition, for a large cavity the shape is not very important in determining the number of modes (although critical for the spatial characteristics of the modes, of course). So for our present purpose we can just as well assume the simplest shape – a cube with sides equal to L . For a cubical cavity Eq. (1.45) becomes

$$\left(\frac{2L}{c} \right)^2 \nu^2 = l^2 + m^2 + n^2. \quad (1.48)$$

It is a useful trick to regard the triplet (l, m, n) as the components of a fictitious vector \vec{q} :

$$\vec{q} = \vec{i}l + \vec{j}m + \vec{k}n \quad (1.49a)$$

with magnitude

$$\vec{q}^2 = q^2 = l^2 + m^2 + n^2. \quad (1.49b)$$

Then the triple integral can be denoted as

$$N = \iiint d^3q. \quad (1.50)$$

Eq. (1.48) indicates that ν depends only on the length, but not the orientation, of the vector \vec{q} . Thus we rewrite the mode integral in spherical coordinates:

$$N = \iiint q^2 dq \sin(\theta_q) d\theta_q d\phi_q \quad (1.51)$$

and carry out the integrations to obtain:

$$N = \frac{4\pi}{8} \int q^2 dq = \frac{4\pi}{8} \frac{q^3}{3}. \quad (1.52)$$

Here the factor 4π is the result of the angular integration and the $1/8$ is due to the restriction on the original integers l, m, n to be positive, so that only the vectors \vec{q} in the positive octant of the integration Eq. (1.50) should be counted as corresponding to the physical modes.

In Eq. (1.49b) q is the length of the vector \vec{q} compatible with the given frequency ν . From Eq. (1.48) it is clear that $q = (2L/c)\nu$, so we finally get

$$N_\nu = \frac{\pi}{6} \left(\frac{2L}{c} \right)^3 \nu^3 = 4\pi \frac{\nu^3}{3c^3} V, \quad (1.53)$$

where $V = L^3$ is the cavity volume.

Since our derivation of Eq. (1.53) did not take into account the polarization of the cavity modes, we are still free to choose any two independent polarizations. Thus we have

$$N_\nu = \frac{8\pi\nu^3}{3c^3} V, \quad (1.54)$$

for the number of possible cavity modes with a frequency less than ν , counting all polarizations.

The number of possible field modes in the frequency interval from ν to $\nu+d\nu$ is therefore

$$dN_\nu = \frac{8\pi\nu^2}{c^3} V d\nu \quad (1.55a)$$

and in the wavelength range $d\lambda$, the number is

$$dN_\lambda = 8\pi \left(\frac{V}{\lambda^3} \right) \frac{d\lambda}{\lambda}. \quad (1.55b)$$

1.3 The modes of an open cavity

It is useful for later discussions to specify the quality factor of the cavity [1.3]. The most general definition is

$$Q = 2\pi \frac{\text{EnergyStored}}{\text{EnergyDissipatedPerCycle}}. \quad (1.56)$$

Physically speaking, Q is 2π times the ratio of the total energy stored, divided by the energy lost in a single cycle, or equivalently the ratio of the stored energy to the energy dissipated per one radian of the oscillation.

We can determine the quality factor by general energy principles. Assume that the distribution of electromagnetic fields inside the cavity is close to that of standing waves and the reflection coefficient of mirrors R . The standing wave equals the two waves with similar intensity and propagating in opposite directions. Let's assume that the power in each standing wave is P . Consequently after reflection from two similar mirrors, these waves will lose $2P(1-R)$ of their starting power P . At the same time the stored energy in the cavity is $2Pl/c$. Therefore from Eq. (1.56) we can find the quality factor:

$$Q = \frac{2\pi l}{\lambda} \frac{1}{1-R}, \quad (1.57)$$

where $R \leq 1$.

Consequently in accordance with the Beer–Lambert law, the influence of the reflecting surfaces is tantamount to an increased propagation distance of a plane wave inside the cavity by a factor $l/(1-R)$.

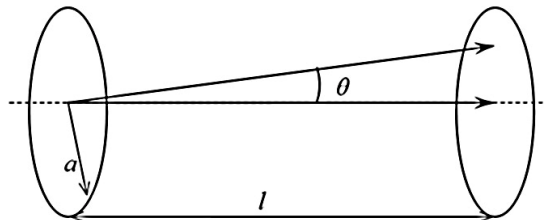


Fig. 1.5. The open resonator consisting of two parallel plane discs.

Let's consider an open resonator consisting of two parallel plane discs with radius a and distance between them l (see Fig. 1.5). In this case the effect

of increasing the propagation distance of a plane wave inside the cavity by $l/(1-R)$ can be considered as e times an attenuation of the given wave after $l/(1-R)$ reflections.

In addition to waves that propagate exactly normal to the mirror surfaces we may expect some waves that propagate almost normal to the surfaces.¹ If a plane wave propagates with some angle to the cavity axis and makes $l/(1-R)$ reflections before leaving the cavity, then regarding Eq. (1.56) the resonance corresponding to this oscillation has a quality factor approximately half than that for normal propagation. Therefore we can determine the angle

$$\theta = 2a(1-R)/l, \quad (1.58)$$

which limits the direction of oscillation of the waves with a high quality factor. Consequently, from all possible oscillations of the open resonator those with the largest quality factor have oscillations with a direction of propagation inside a solid angle of $\Omega = \pi\theta^2$.

The product of $\Omega/4\pi$ and Eq. (1.55a) is the number of oscillations with a high quality factor in the frequency interval $\Delta\nu$.

$$N_0 = 32\pi^2 \frac{(1-R)^2}{\lambda^3 l} \frac{\Delta\nu}{\nu}, \quad (1.59)$$

where $\lambda = c/\nu$ is the wavelength.

¹ The number of normal and non-normal waves available in a cavity is infinite (see Eq. 1.49). However, the number of waves whose frequency lies in the neighborhood $d\nu$ of a given value ν is finite (see Eq. 1.63). All normal or non-normal propagating waves must satisfy the boundary conditions due to this factor in a cavity can oscillate an integer number of waves which propagate normally to the mirrors surface and an integer number of waves which can propagate non-normally to the surface. These waves we call characteristic oscillations or resonance oscillations or modes of the resonator. The set of characteristic oscillations which propagate normally to the mirrors of a cavity are called the longitudinal modes of the resonator and the set of modes which has non-normal direction of propagation are radial modes of the resonator.

The boundary condition can allow the existence of characteristic oscillations which have angular rotation by $2\pi n$ times inside the resonator (the angular modes of the resonator). Due to the form of the boundary conditions, the modes propagate with no rotation and with $2\pi n$ angle rotation are similar. Depending on the number of rotations relative to the axe of the cavity, the mode has order n . For example if during the propagation inside the cavity from one mirror to another the mode rotates the phase by 4π . This mode has a 2nd angular order. A similar situation and with a radial mode order, the 1st order of the radial mode means this mode has the smallest non-normal angle of propagation in the cavity.

Generally all cavity modes (for cylindrical coordinate systems which are the most suitable for open resonators with our geometry (see Fig. 1.5)) have longitudinal, radial and angular orders at the same time and can be presented by three integer numbers m, n, l . (similarly to Cartesian coordinates (see Eq. 1.45 (a-c))) Each number is presenting the spatial order of the mode in a suitable coordinate system.

The comparison of Eq. (1.59) and Eq. (1.55a) leads to a dramatic $l^2 / (a^2(1-R)^2) \gg 1$ times decrease in the number of characteristic oscillations in the case of an open resonator. The source of this behavior is due to the absence of side walls in the open resonator.

We are now able to define some useful relationships that may be derived from Eq. (1.59). These are listed as follows:

The frequency interval corresponding to only the resonance oscillation:

$$\frac{\Delta\nu}{N_0} = \frac{\lambda^3 l \nu}{32\pi^2 a^4 (1-R)^2}. \quad (1.60)$$

The frequency width of only the resonance oscillation will be defined by the quality factor:

$$\Delta\nu_k = \frac{\nu}{Q} = \frac{\lambda\nu(1-R)}{3\pi d}. \quad (1.61)$$

The resonance curves of different oscillations have no overlap according to Eq. (1.60) and Eq. (1.61):

$$\frac{\Delta\nu_k}{\Delta\nu/N_0} = 16\pi N_F^2 (1-R)^3 < 1, \quad (1.62)$$

where $N_F = a^2/l\lambda$.

We can see from Eq. (1.62) that for mirrors of an open resonator with a high reflectivity and accordingly high quality factor, it is possible to reach sufficient decimation of the spectrum of characteristic oscillations, even though the Fresnel number is high.

1.4 The stability of an open cavity

Lets consider a waveguide consisting of a set of thin lenses with equal focal lengths, width and distances between them (see Fig.1.6) [1.3]. Because of the reflection from the resonator mirror, in principle, is identical to transmitting through a lens of similar focal length and width. We can suppose that this scheme is equivalent to the open cavity.

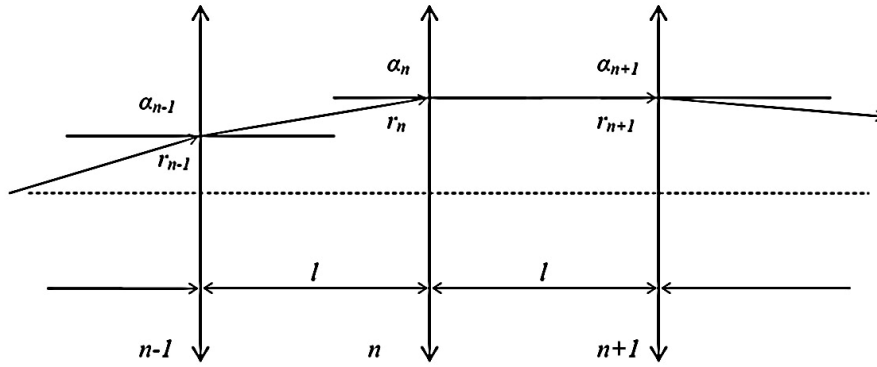


Fig. 1.6. The representation of an open cavity by waveguides consisting of a set of thin lenses.

Assume that the trace of the rays through this system obeys the paraxial approximation; consequently we may make use of the well-known lens equation:

$$1/a_1 + 1/a_2 = 1/F, \quad (1.63)$$

where a_1 – the object distance, a_2 – the image distance and F – the focal length of the lens.

We can rewrite this equation in paraxial approximation for $r \ll a_1, a_2$ namely:

$$\alpha_1 - \alpha_2 = r/F, \quad (1.64)$$

where r is the distance from the optical axis to the point where the ray intersects the lens, and α_1 and α_2 are the incident and refracted angles respectively (see Fig. 1.7).

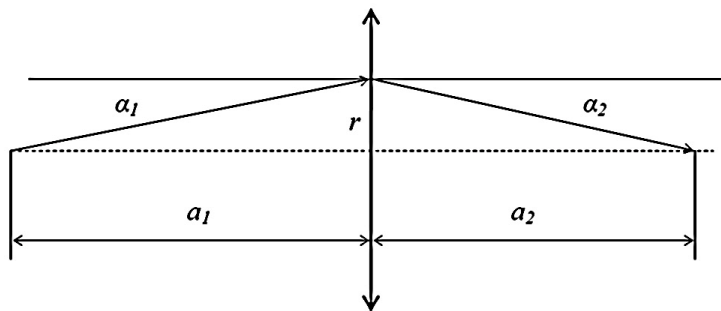


Fig. 1.7. The angles of the light ray before and after passing through the thin lens.

Lets consider the three neighboring lenses, labeled $n-1, n$ and $n+1$. Then:

$$\alpha_n - \alpha_{n-1} = r_n/F. \quad (1.65)$$

At the same time the distance from the ray up to the lens axis is

$$r_{n-1} = r_n + \alpha_n l, \quad r_n = r_{n-1} + \alpha_{n-1} l. \quad (1.66)$$

Subtracting the first equation from the second leads to the following recurrence formula:

$$r_{n-1} + (l/F - 2)r_n + r_{n+1} = 0, \quad (1.67)$$

which allows one to determine the position of the ray on any lens in the system if the positions on the two previous lenses are known. The method of sequential passes of the ray inside the resonator, corresponding to the recurrence formula (1.67), is similar to the well known Fox-Li method [2.2].

It is possible to solve Eq. (1.67) analytically by assuming a solution of the form:

$$r_n = A \exp(in\theta), \quad (1.68)$$

where A is a constant. Substituting Eq. (1.68) into Eq. (1.67), and requiring that both the imaginary and real parts must be of the solutions, yields:

$$\cos(\theta) = 1 - l/2F. \quad (1.69)$$

The last equation is the partial solution of Eq. (1.67). By considering this partial solution we can conclude that the waveguide (see Fig. 1.7) is stable if r_n oscillates within the limits $\pm A$, where A is the initial position of the ray in the waveguide.

Consequently the continuing oscillations exist when θ is real or $\cos(\theta)$ is within the limits ± 1 and the variation of the admissible region of l/F is determined by following inequality:

$$-1 \leq 1 - l/2F \leq 1. \quad (1.70)$$

By following the same steps, we can easily derive similar inequalities, but for waveguides which have two types of lenses with different focal lengths following each other

$$0 \leq (1 - l/2F_1)(1 - l/2F_2) \leq 1. \quad (1.71)$$

Eq. (1.71) is the more general case of the stability condition of an open cavity with different focal lengths of the lenses, and is equivalent to Eq. (1.70) when the lenses are identical.

By introducing two new parameters defined as $g_1 = 1 - l/2F_1$ and $g_2 = 1 - l/2F_2$, the boundary of the accepted values for l and F must satisfy:

$$g_1 g_2 = 1 \quad (1.72a)$$

$$g_1 g_2 = 0 \quad (1.72b)$$

Eqs. (1.72) allow the simple graphical representation of the stability region of an open cavity (see Fig. 1.8). Areas bounded by the line $g_1 g_2 = 1$ as well as the axes are stable.

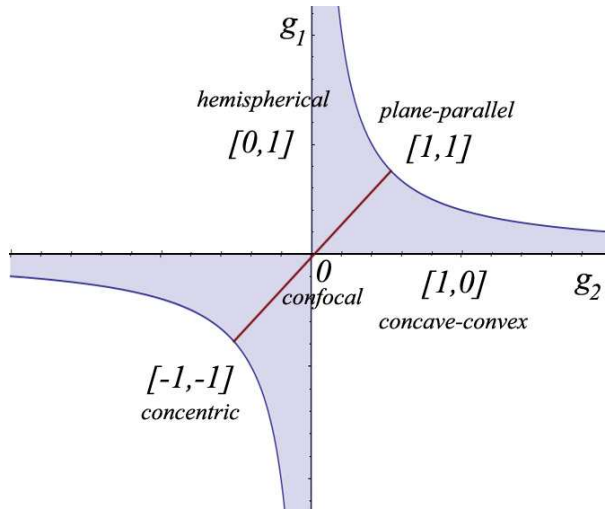


Fig. 1.8. The stability region of an open cavity.

1.5 The Fresnel number of a cavity

Since the above analysis did not include diffraction, it is not possible to discuss diffraction losses [1.3]. To do so one requires the introduction of propagating plane waves. In accordance with Young's representation, the diffraction due to the edge of a screen can be described as transverse amplitude diffusion. At a distance l from the screen, the diffusion region is around $\sqrt{l\lambda}$. Consequently, the beam with a field close to a plane wave, after a reflection from the left mirror, having a radius a , increases the beam radius by $\sqrt{l\lambda} \ll a$.

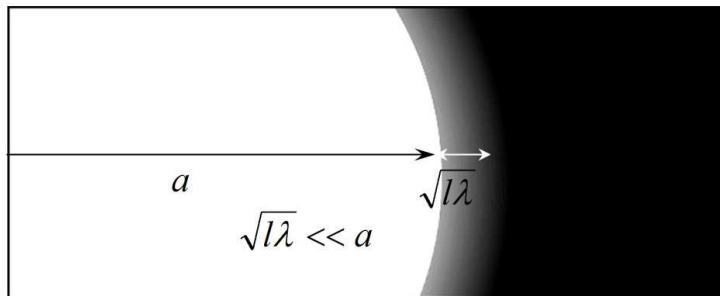


Fig. 1.9. Young's representation of the diffraction on a round screen.

The radiation, associated with a ring of area $2\pi a \sqrt{l\lambda}$, leaves the resonator [see Fig. 1.9]. Since the plane waves have a constant amplitude, we may

estimate this loss as $2\sqrt{l\lambda}/a$. After squaring this value, we are able to make an estimate of the energy loss after one pass:

$$A_{\text{Diff}} = \frac{4l\lambda}{a^2} = 4/N_F, \quad (1.73)$$

where $N_F \equiv a^2/l\lambda$ is the Fresnel number of the resonator. Consequently larger Fresnel number resonators will have smaller diffraction losses.

The aforementioned estimate of diffraction losses is correct for large Fresnel numbers, but because the field distribution in a real resonator is not uniform and drops rapidly at the edges, the actual diffraction loss is in reality less than predicted by Eq. (1.73). Consequently, the estimate of the tendency of dependency of the diffraction losses from the Fresnel number is more correct.

Chapter 2

Fox–Li mode development analysis and a matrix method

In this Chapter we will consider the well-known integral iteration algorithm for intra-cavity field simulation, namely the Fox–Li algorithm [2.1, 2.2] and a new method (matrix method), which is based on the Fox–Li algorithm and can decrease the computation time of both the Fox–Li algorithm and any integral iteration algorithms.

In general, the time taken for the calculation is the weakest part of the integral iteration algorithms. Consequently, the development of mathematical methods is an important task which will decrease the computation time and can strongly simplify the solution. In this Chapter we will present a novel method which can considerably decrease the computation time of the integral iteration algorithms, without loss of precision.

The method which we will describe below can be used for any class of integral iteration algorithms which have the same calculation integrals, with changing integrands (where the integrand is the field of the light wave in the case of the Fox-Li algorithm (see Sec. 2.1), IFTA (see Sec. 2.2), and screen method (see Sec. 2.3)). The given method appreciably decreases the computation time of these algorithms and approaches that of a single iteration computation.

2.1 Fox–Li algorithm

The Fox-Li algorithm is used for computing the intra-cavity field. For that we have to calculate the field on one of the mirrors through the Fresnel integral, with a random field (the simulation of random process of mode development by spontaneous emission in the active medium of a laser) on the opposite mirror (see first part of Eq. (2.1) with $u_2(x)$ –random function), and then we have to calculate the field on the opposite mirror taking into account the previous field

using the same Fresnel integral and so on, until the intra-cavity field approaches a steady state (see Fig. 2.1).

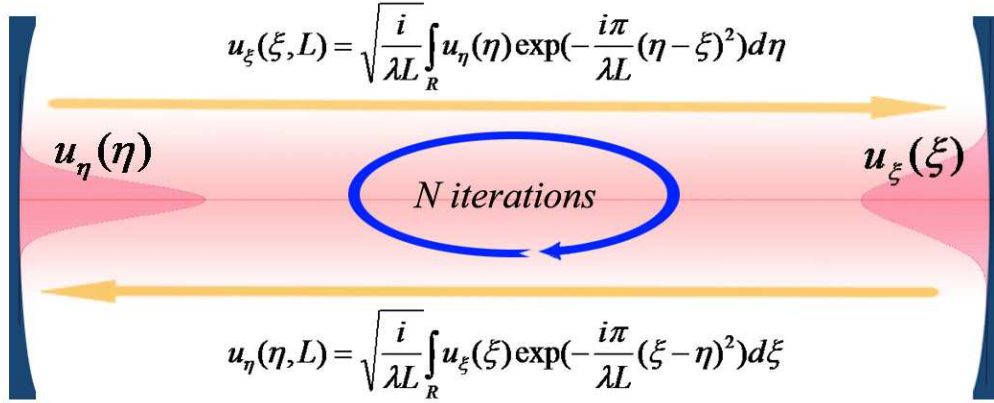


Fig. 2.1. The illustration of Fox–Li method.

The number of iterations of the Fox–Li algorithm depends on the Fresnel number [see Sec. 1.5]. In the case of small Fresnel number for a given resonator, we will need less computation iterations to approach the steady state and vice versa.

2.2 Matrix method

The central idea to the so-called Matrix Method approach is to note that only the integrand of the two propagation integrals (one for each direction) is changing on each pass of the resonator, and not the kernel itself. Therefore, if the transformation of a field on passing through the resonator could be expressed as the product of two matrices – one representing the starting field and the other the transformation of that field – only the former would have to be calculated on each pass, and not the latter.

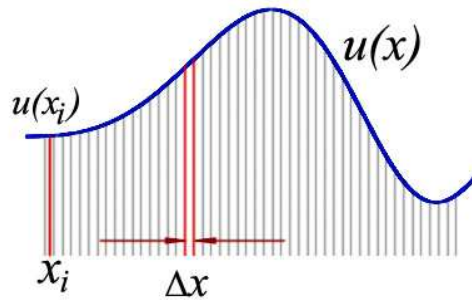


Fig. 2.2. Illustration to the matrix method development.

To illustrate the method, consider sub-dividing of two mirrors into N parts each with size $\Delta x = 2X_2/N$ for mirror M_2 and, $\Delta x = 2X_1/N$ for mirror M_1 , where X is the radius of the respective mirrors. If Δx is small enough, then the field $u(x)$ across that segment of the mirror may be assumed to be constant (see Fig. 2.2). We can now divide the Fresnel integral into a sum of integrals over each segment of mirror. As each segment has constant amplitude (albeit a different constant), this term may be removed from the integral, which in the case of propagating from mirror M_2 to M_1 becomes [2.3]:

$$\begin{aligned}
 u_1(x_1, L) &= \sqrt{\frac{i}{\lambda L}} \int_{-\infty}^{\infty} u_2(x_2) \exp\left(-\frac{i\pi}{\lambda L}(x_1^2 - 2x_1x_2 + x_2^2)\right) dx_2 \\
 &= \sum_{i=0}^N u_2(X_2 - i\Delta x) \int_{X_2 - i\Delta x}^{X_2 - (i+1)\Delta x} \sqrt{\frac{i}{\lambda L}} \exp\left(-\frac{i\pi}{\lambda L}(x_1^2 - 2x_1x_2 + x_2^2)\right) dx_2.
 \end{aligned} \tag{2.1}$$

Since the integrand in Eq. (2.1) does not change with the changing field, we may express Eq. (2.1) in matrix form as

$$\vec{u}_1 = T \vec{u}_2, \tag{2.2}$$

where

$$\vec{u}_1 = \begin{pmatrix} u_1(X_1) \\ \cdot \\ u_1(X_1 - n\Delta x) \\ \cdot \\ u_1(-X_1) \end{pmatrix}, \tag{2.3}$$

$$\vec{u}_2 = \begin{pmatrix} u_2(X_2) \\ \cdot \\ u_2(X_2 - n\Delta x) \\ \cdot \\ u_2(-X_2) \end{pmatrix}, \tag{2.4}$$

$$T = \begin{pmatrix} T_{11} & T_{12} & \cdot & \cdot & T_{1N} \\ T_{21} & T_{22} & \cdot & \cdot & \cdot \\ \cdot & \cdot & \cdot & \cdot & \cdot \\ \cdot & \cdot & \cdot & \cdot & \cdot \\ T_{N1} & \cdot & \cdot & \cdot & T_{NN} \end{pmatrix} \tag{2.5}$$

and

$$T_{ij} = \int_{X_2 - n\Delta x}^{X_2 - (n+1)\Delta x} \sqrt{\frac{i}{\lambda L}} \exp\left(-\frac{i\pi}{\lambda L}(x_1^2 - 2x_1x_2 + x_2^2)\right) dx_2. \tag{2.6}$$

This approach dramatically decreases the computation time, since the elements of the transfer matrix, T , need be calculated only once. If the mirror segments are sufficiently small we may further reduce the Riemann integrals in T as

$$T'_{ij} = \lim_{\Delta x \rightarrow 0} T_{ij} = \sqrt{\frac{i}{\lambda L}} \exp\left(-\frac{i\pi}{\lambda L}(x_1^2 - 2x_1x_2 + x_2^2)\right) \Delta x, \quad (2.7)$$

and thus decreasing the computational time further. For a non-symmetrical cavity, as is the case in this study, one is required to calculate the forward and reverse propagation matrices separately. The method may also be extended to multi-element resonators by application of a suitable Collins integral [2.4] in Eq. (2.1).

For the first step of the matrix method (see Eq. (2.6)) the complex amplitude of the optical field is taken to be approximately constant, but for the second step (see Eq. (2.7)) this consideration is inadequate. The integrands of all Fresnel integrals of matrix T need to be constant. In most cases, this will usually lead to an increase in the matrix sizes. Consequently, in order to decide which representation we have to choose we must analyse the behavior of all the integrands and the amplitude functions. For example, to simulate the field behavior in an open resonator with mirror diameters of 1 cm and a distance between the mirrors of 0.3 m at a wavelength of 1.064 μm we have to divide a mirror into 10^3 parts. This will give us a good description of this system by the Fresnel matrix (see Eq. (2.6)) which will consist of 10^6 elements. At the same time, to describe the same system by the integral free Fresnel matrix (see Eq. (2.7)) we must have 10^4 divisions at least and consequently 10^8 elements.

All calculations of the Fresnel integral employing the Fox-Li method, have been presented as a multiplication of two matrices only and the computation time of the field distribution inside the resonator decreases and takes approximately the same calculation time as the Fresnel integral for a single pass.

If we write the matrices for the forward and backward propagation directions inside the resonator as T_1 and T_2 respectively, then the characteristic integral equation for any resonator system can be presented in the terms of the matrix method as:

$$\lambda \vec{u}_1 = T_1 T_2 \vec{u}_1. \quad (2.8)$$

Eq. (2.8) has solutions if the determinant of $I\lambda - T_1T_2$ is zero; consequently all eigenvectors of T_1T_2 represent the possible resonator modes, while all eigenvalues represent the losses with phase shift for these corresponding modes. The method was applied to the computation of a Bessel-Gauss, Flat-Top and Gaussian cavity and it decreases computation time of Fox-Li method considerably [4.13, 5.13, 5.15 and 5.17].

2.3 Other applications

Generally the matrix method can be adapted to any integral iteration algorithms. In this Chapter we will consider two well known iteration algorithms: the popular iterative Fourier transform algorithm (IFTA) for diffraction optical elements (DOE) shape calculations [2.5] and the phase screen method for generation of turbulence transformation of the optical field based on Noll's representation of near field Kolmogorov phase modification [2.6].

2.3.1 Iterative Fourier transform algorithm

The given algorithm was applied to a well known popular method of computation of surface profile (phase pattern) of DOE known as the iterative Fourier transform algorithm (IFTA). The general description of IFTA algorithm follows. The intensity distribution, which can be Gaussian or otherwise, formed from the incident beams and the initial random surface profile of the DOE are first determined. After the beams have propagated to a given point (image plane) using forward Fourier transformation (FFT), the amplitude only is replaced by the amplitude of an ideal intensity distribution. The beams are then propagated in the reverse direction using reverse Fourier transformation (RFT), the altered surface profile is left as is, and the amplitude is replaced by the amplitude of a Gaussian intensity distribution and so on [2.5, 2.7] (see Fig. 2.3).

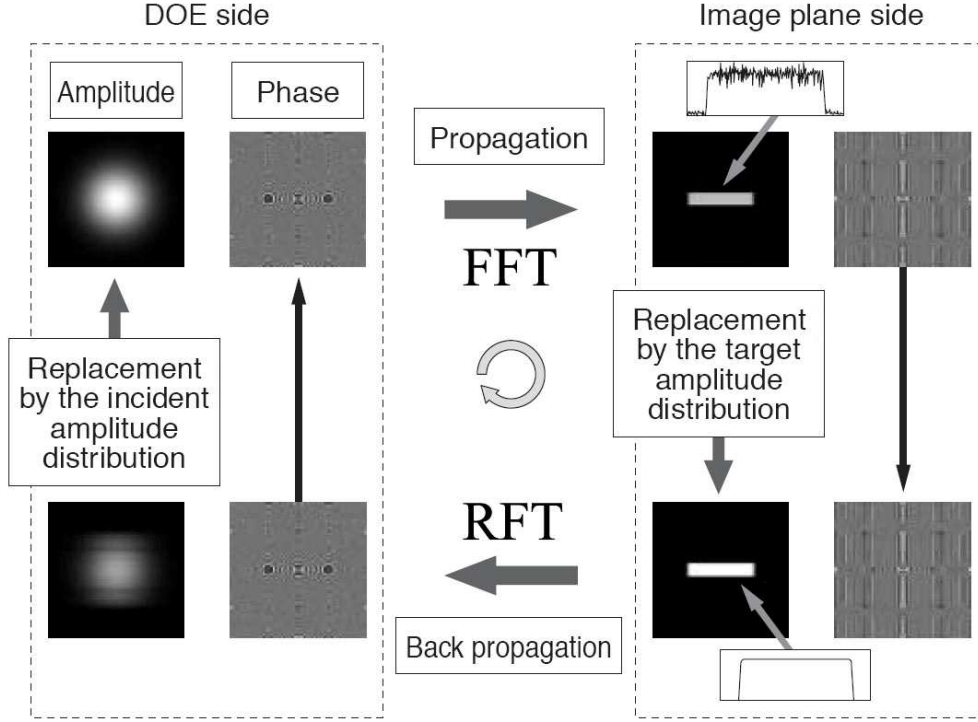


Fig. 2.3 The Iterative Fourier transform algorithm.

As we can see in the given case we have to calculate forward and inverse Fourier transformation every pass of the iteration algorithm. Consequently we can apply the matrix method, described above, but in the given case we have to find two integral matrices: one matrix is for forward transformation and the other is for inverse Fourier transformation. Integral matrices for the one dimensional case for forward and inverse Fourier transformation which take into account the approximation of a practically constant integrand (see above method) will be:

$$B_F = \begin{pmatrix} I_F^{a_{11}} & I_F^{a_{12}} & \cdot & \cdot & I_F^{a_{1N}} \\ I_F^{a_{21}} & I_F^{a_{22}} & \cdot & \cdot & \cdot \\ \cdot & \cdot & \cdot & \cdot & \cdot \\ \cdot & \cdot & \cdot & \cdot & \cdot \\ I_F^{a_{N1}} & \cdot & \cdot & \cdot & I_F^{a_{NN}} \end{pmatrix}, \quad (2.9a)$$

where

$$I_F^{a_{ij}} = \frac{\exp(ikf)}{\sqrt{i\lambda f}} \exp\left(i\frac{k}{L}x_jx_i\right)\Delta x. \quad (2.9b)$$

Or for inverse Fourier transform:

$$I_{F^{-1}}^a{}_{ij} = \frac{\exp(ikf)}{\sqrt{i\lambda f}} \exp(-i\frac{k}{L}x_jx_i)\Delta x. \quad (2.9c)$$

2.3.2 The simulation of turbulence transformation of the optical field

To illustrate the method we can consider one more integral iteration algorithm for the simulation of the atmospheric turbulence. This is the phase screen method for the generation of turbulence transformation of an optical field. The phase screens will be calculated by decomposing the phase function, where the phase function represents the near field Kolmogorov turbulence phase transformation. It is decomposed into a series of Zernike polynomials by following the Noll representation of Zernike coefficients for the Kolmogorov view of the statistic structure function [2.6]. To generate the phase and amplitude transformation of the optical field over a certain propagation distance we will use a phase screen technique which is based on the division of beam paths into parts for which we can consider the variation of optical field as a near field transformation. Consequently, to produce the optical field modification we can apply the Fresnel transformation as well as multiplication of the initial optical field by the Noll representation of turbulence phase change on every part of the division.

From the above discussion we can now see that for each part of the optical path we have to calculate the same Fresnel integral but only change the integrand, namely the optical field, by multiplying by the turbulence phase change. We are now able to use the matrix method described above. We can simulate the Fresnel matrix once and all the field modifications during propagation will be represented by the multiplication of three matrices, namely the constant Fresnel matrix and two varying matrices: the phase transformation turbulence matrix and the amplitude matrix:

$$A_{t+1} = A_t T_t B, \quad (2.10)$$

where t is the number of phase screens, A is the complex amplitude matrix, T is the phase transformation turbulence matrix and B is the Fresnel transformation matrix.

2.4 Conclusion

In this Chapter a method was presented which decreases computation time of integral iteration algorithms by the examples of both Fox-Li method and IFTA. This method was applied successfully by the author in calculating Bessel-Gauss, Flat Top, Gaussian and Bessel-like beam cavities [4.13, 5.13, 5.15 and 5.17]. The speed of calculation of this method approaches the speed of calculation of a single pass of the integral iteration algorithm. For the case of Fox-Li algorithm the method is able both to reduce the calculation time and able to show the transverse field distribution of all possible resonator modes and the losses with phase shift for these corresponding modes as well (see Eq. 2.8).

Chapter 3

Petal-like modes in Porro prism resonator

To overcome misalignment problems and to raise stability of resonator systems, Porro prisms can be used instead of resonator mirrors. The employment of Porro prisms leads to unique behavior of the output beam profile. For this type of cavity the influences of losses on the apexes of the Porro prisms and the angle between them have a dominant influence on the transverse intensity profile of the output beam. Consequently we have one of the cases of amplitude intra-cavity beam shaping. In this Chapter a new approach to modeling the spatial intensity profile from Porro prism resonators is proposed based on rotating loss screens to mimic the apex losses of the prisms. A numerical model based on this approach is presented which correctly predicts the output transverse field distribution found experimentally from such resonators.

3.1 Introduction

Right angle prisms, often referred to as Porro prisms, have the useful property that all incident rays on the prism are reflected back parallel to the initial propagation direction, independent of the angle of incidence. Thus an initial planar wave front remains planar after reflection. This property was initially exploited in Michelson interferometers to relax the tolerances on misalignment, and then proposed in 1962 by Gould *et al* [3.1] as a means to overcome misalignment problems in optical resonators employing Fabry-Perot cavities by replacing the end face mirrors with crossed roof prisms. Lasers based on this principle have been developed over the years [3.2-3.6] with a review of the basic concepts and literature for Porro prisms specifically found in [3.7]. Much of the theoretical work to date has focused on geometric methods to model the inverting properties of such resonators [3.2-3.4] and polarization considerations to account for internal phase shifts and output polarization states [3.6,3.7]. In

[3.2] the prism was modeled as a ray deviator by replacing an imaginary mirror some distance behind the prism. The model correctly accounted for the beam direction, but did not account for the complex field distribution found experimentally from the laser.

In [3.4] the relative change of the beam pointing direction for a misaligned Porro prism resonator is analyzed. A concept of the oscillation axis for the Porro prism resonator is introduced to find the beam direction. Expressions for the beam tilting angles are deduced. They predict that the angular misalignment in the horizontal direction will lead to beam tilting in both the horizontal and vertical directions.

An electro-optically Q-switched Nd:YAG laser resonator that uses two end prisms placed orthogonally perpendicular to each other has been designed in [3.6]. This configuration improves the stability of the resonator and does not alter the characteristics of the electro-optical Q switch. The out-coupling ratio of the cavity is optimized by a change in the azimuthal angle of a phase-matched Porro prism placed at one end of the cavity. The prism placed at the other end of the cavity is designed so that it introduces a phase change of P , regardless of its orientation and index of refraction, resulting in a more efficient and stable cavity.

The physical optics models fail to account for the true field pattern found from such resonators [3.3, 3.8]. In [3.3] for example, the kernel of the Fresnel-Kirchoff diffraction integral contains only the optical path length experienced by the beam, thus treating the prism as though it were acting like a perfect mirror, with an identical ABCD matrix representation albeit incorporating the inverting properties of the prisms. This approach appears to be the preferred model for prisms, even though it does not explain the complex transverse field patterns found in Porro prism resonators. This is a recurring problem in the literature, with only a hint at a solution offered in [3.8] and [3.9], where it was proposed to treat the field patterns as a result of diffractive coupling between a linear combination of sub-resonators. Anan'ev [3.9], in considering the theoretical properties of resonators with corner cube prisms, specifically mentioned the influence of bevels of finite width at the prism edges as a possible explanation for a tendency for distinct longitudinal sectors to oscillate

independently, but did not go on to develop this idea into a model which could be used to explain experimental results.

In this Chapter we outline a new method for modeling the transverse field patterns observed from crossed Porro prism resonators [3.11]. The model departs from earlier attempts in that the prisms are modeled as rotating elements with amplitude and phase distortions, and incorporates both physical optics and geometrical optics concepts. The model is developed in Section (3.2) and its properties discussed, and then applied in Section (3.3) to the case of a marginally stable crossed Porro prism resonator with a polarizer as an output coupler.

3.2 Porro resonator concept

A typical Porro prism resonator is shown in Fig. 3.1. Consider for the moment only the two Porro prisms and how they impact on the propagating field. Imagine viewing the resonator along its length from one prism (element **h**) looking towards the other (element **a**). On encountering a prism, the field inverts itself around the prism apex, and reverses its propagation direction, traveling back towards the opposite prism. The same inversion and reversing of propagation direction takes place again, and this sequence repeats on each pass. The prisms would essentially be treated as perfect mirrors but with a field inverting property.

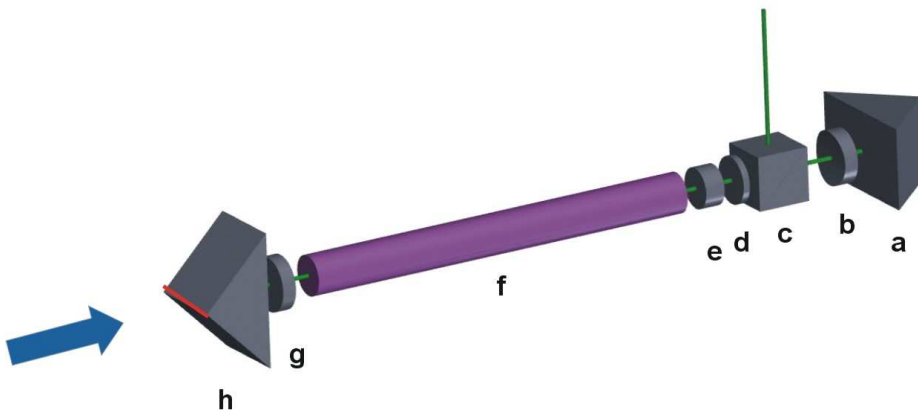


Fig. 3.1. A typical Porro prism based Nd:YAG laser with passive Q-switch, showing the following optical elements: Porro prisms (elements **a** and **h**); intra-cavity lenses (elements **b**

and g); a beamsplitter cube (element c); a quarter wave plate (element d), and a passive Q-switch (element e).

Our approach to modeling a resonator containing Porro prisms is to describe the prisms as standard mirror elements, but with associated amplitude and phase screens, as illustrated in Fig. 3.2. These screens act on the incoming field by modifying both its amplitude and phase by means of a suitable optical transfer function $t(x,y)$:

$$U_{out}(x,y) = U_{in}(x,y)t(x,y) = U_{in}(x,y)A(x,y)\exp(i\phi(x,y)), \quad (3.1)$$

where $A(x,y)$ describes the amplitude effects and $\phi(x,y)$ describes the phase effects of the prism respectively. In the case of a Porro prism, the amplitude screen introduces losses not only at the edges of the element (transverse confinement), but also at the small but significant bevel along the apex where the prism surfaces meet. The phase screen allows for the optical path length to vary as a function of the input position on the prism face, for example, to model errors in the prism angle or fabrication errors on the prism surfaces. With this approach, the diffractive effects of the prisms are taken into account, and the screens can be treated as intra-cavity elements that change the eigenmodes of a standard mirror-mirror resonator. Here we employ only the amplitude screen approach to model perfect prisms with high losses where the prism edges meet. The transfer function for the new prism model then includes only the amplitude effects, $t(x,y) = A(x,y)$, and describes a high loss region along the apex of the prism, with 100% losses, and no losses elsewhere within the clear aperture of the element.

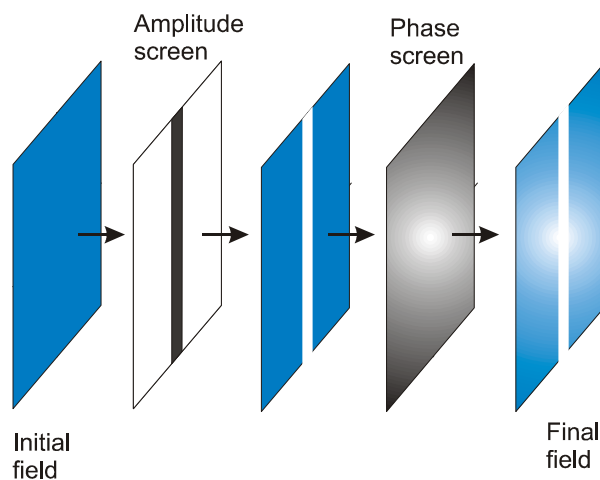


Fig. 3.2. Illustration of the effect of phase and intensity screens on an incident field.

A geometric approach is useful in understanding the symmetry and repeatability of the resonator modes: consider a propagating ray viewed along the optical axis and assume, without any loss of generality, that the Porro prism (PP) closest to the observer has its apex in the horizontal plane, while the opposite PP has its apex rotated at some angle α from the horizontal, which we will refer to henceforth as the *Porro angle*. By way of example, we consider the case of $\alpha = 60^\circ$, as illustrated in Fig. 3.3 (a–e). In the analysis to follow the pertinent information is the location of the prism apexes, which we illustrate as solid lines 1 and 2 in Fig. 3a, corresponding to elements *h* and *a* in Fig. 3.1 respectively.

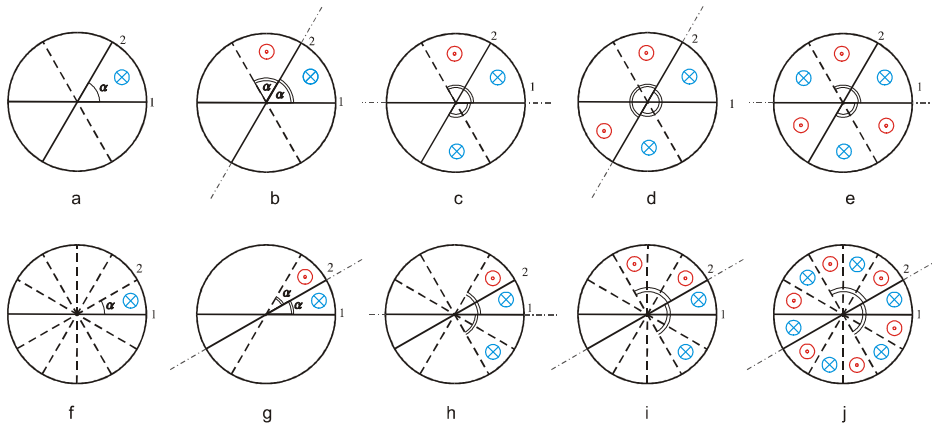


Fig. 3.3. (a) – (e): Evolution of a ray as it is reflected back and forth in the resonator, for starting Porro angle $\alpha = 60^\circ$. After 3 round trips the pattern is complete (e) and starts to repeat. (f) – (j): Equivalent case but with $\alpha = 30^\circ$, and now taking 6 round trips for completion.

We have *a priori* knowledge of how the mode will develop, and hence start with a ray located as shown in Fig. 3.3 (a), traveling away from the viewer towards PP 2. We have chosen this location based on the assumption of high loss along the apexes, thus avoiding the apex zones. At PP 2 the ray is inverted about the prism apex, and travels back towards the viewer parallel to the optical axis as indicated in Fig. 3.3 (b). At PP 1, the ray is inverted about the prism axis, and travels back towards PP 2 (see Fig. 3.3 (c)). This process continues until the complete pattern is created (see Fig. 3.3 (e)), and the ray has returned to its starting position. This happens after three round trips. Clearly subsequent reflections simply duplicate the pattern. A second example is shown in Fig. 3.3 (f) – (j), where we illustrate the case of $\alpha = 30^\circ$. The same propagation rules apply so that eventually, after six complete round trips the pattern starts repeating itself. Clearly this approach correctly predicts the observed petal pattern formation often observed from such lasers, but this is based on *a priori*

knowledge and not physical reasoning. Also, this approach is only useful for limited Porro angles.

An alternative approach, which is more useful in modeling such a resonator, is to consider that since losses are introduced onto the field from each prism apex, and the field is then inverted, one can view the situation as the amplitude screen being inverted after each prism reflection. From the viewpoint of the field traveling inside the resonator, the equivalent picture is that of the field remaining inversion free, while the prisms themselves invert after each pass, essentially appearing to rotate by an amount dependent on the Porro angle, and hence the main area of losses (the apex edges) also appear to rotate. An example of this rotation is shown in Fig. 3.4.

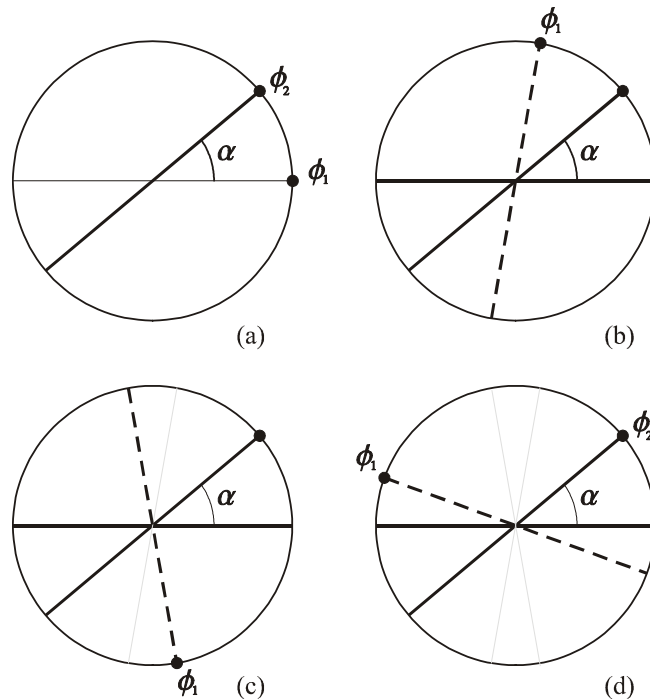


Fig. 3.4. The apices of two Porro prisms at angles ϕ_1 and ϕ_2 . Initially the apex of PP 1 is in the horizontal plane (a), but after successive reflections about the inverting edges of the two prisms the apex will appear to be rotating about the circle: (b) 1 pass, (c) 2 passes and (d) 3 passes.

In order to develop a physical optics model based on this approach, we need to have expressions for the equivalent picture of the rotating prism apices (high loss areas). Consider the rotation of the first PP apex, which we shall denote with the subscript 1, whose position on the circle in Fig. 3.4 we describe by the vector $v_1 = (x_1, y_1)$ with angular displacement given by ϕ_1 . The region of high loss is then simply a line passing through the origin with slope y_1/x_1 . Without any loss of generality we will assume the resonator is viewed such that the first

PP has an edge parallel to the horizontal axis, with the second PP rotated at the Porro angle, as illustrated in Fig. 3.1. It is easy to show that after n reflections this vector has rotated through an angle $\theta_1(n)$ given by:

$$\theta_1(n) = (-1)^{n+1} 2n\alpha, \quad (3.2)$$

where α is the Porro angle. The angular position of this vector after n reflections can be found from:

$$\phi_1(n) = \sum_{i=0}^n \theta_1(i) = \frac{\alpha}{2} [1 - (-1)^n (1 + 2n)]. \quad (3.3)$$

Prior to any reflections the apex of the first prism is at $\phi_1(0) = 0$, so that if we imagine the apexes rotating about the unit circle, then the vector $v_1(n)$ may be expressed as:

$$v_1(n) = \begin{pmatrix} \cos \phi_1(n) & -\sin \phi_1(n) \\ \sin \phi_1(n) & \cos \phi_1(n) \end{pmatrix} \begin{pmatrix} 1 \\ 0 \end{pmatrix}. \quad (3.4)$$

Similar expressions can be derived for the second PP apex, which we state here for the convenience of the reader:

$$\theta_2(n) = (-1)^n 2n\alpha, \quad (3.5)$$

$$\phi_2(n) = \alpha - \frac{\alpha}{2} [1 - (-1)^n (1 + 2n)]; \quad (3.6)$$

$$v_2(n) = \begin{pmatrix} \cos \phi_2(n) & -\sin \phi_2(n) \\ \sin \phi_2(n) & \cos \phi_2(n) \end{pmatrix} \begin{pmatrix} 1 \\ 0 \end{pmatrix}, \quad (3.7)$$

Note that the notation has been selected so that the initial positions of the two apexes are given by:

$$v_1(0) = \begin{pmatrix} 1 \\ 0 \end{pmatrix}, \quad (3.8a)$$

$$v_2(0) = \begin{pmatrix} \cos \alpha \\ \sin \alpha \end{pmatrix}, \quad (3.8b)$$

with corresponding initial apex loss regions along $y_1 = 0$ and $y_2 = (\tan \alpha) x_2$ respectively.

A consequence of this model is that only at some discrete starting angles, α , will the rotating edges repeat on themselves. At these angles the field is finitely subdivided by the prisms losses, and it takes a certain number of passes for the subdivision of the field to be complete. The resulting field is then made up of a circular pattern of spots which we refer to as petals or as a petal pattern. At

other angles, the edges never repeat on themselves, thus infinitely sub-dividing the field. With this formalism we are able to find the angles α at which these repeating patterns manifest themselves, as well as the number of sub-divisions (or equivalent, number of petals) that will be observed. Consider for example the first Porro prism apex. It will return on itself when $v_1(n) = v_1(0)$, which leads from Eq. (4) to the relation:

$$\begin{pmatrix} \cos \phi_1(n) & -\sin \phi_1(n) \\ \sin \phi_1(n) & \cos \phi_1(n) \end{pmatrix} = \begin{pmatrix} 1 & 0 \\ 0 & 1 \end{pmatrix}. \quad (3.9)$$

This will be true when

$$\phi_1(n) = \frac{\alpha}{2} [1 - (-1)^n (1 + 2n)] = i2\pi, \quad (3.10)$$

for any integer i . By selecting only the positive solutions for α , one can derive a simple expression for the initial angles α , that will lead to a finitely sub-divided field (or repeating pattern from the geometric viewpoint):

$$\alpha = \frac{i\pi}{m}, \quad (3.11)$$

for any positive integers i and m . The same result can be derived by starting from vector v_2 . The implication is that only at these specific angles α will the field be finitely sub-divided, thus leading to some regions with low loss for lasing. In addition, since the position of these sub-divisions remains stable (i.e., they repeat on themselves) after a certain number of round trips, the modal pattern that oscillates inside such a resonator will give rise to a petal pattern *only* at those angles given by Eq. (3.11). At other Porro angles the high loss apexes will continuously rotate to new positions, thus resulting in high losses across the entire field. We can now go on to calculate how many petals will be observed for a given Porro angle α . The number of petals will be equal to the number of sub-divisions of the field, but the field may not be completely sub-divided in one complete rotation of the vector; it may take several complete rotations for this to happen. We note that the sub-divisions will not necessarily be equal to the Porro angle; when several rotations of around the circle are needed to complete the sub-divisions, it is likely that the area between the initial apexes will be sub-divided further. In general, write the following expression relating the Porro angle to the total number of sub-divisions (petals) of the field:

$$\frac{\alpha}{j} = \frac{2\pi}{N}. \quad (3.12)$$

The validity of this is evident from the following heuristic argument: The complete circle (2π) divided by the total number of sub-divisions N must return the angle of each sub-division. If the sub-division is completed in one rotation, then the sub-division angle will equal α , but if more complete rotations are needed, then this will result in α itself being sub-divided by integer amount, j . Thus both the left and right hand sides of Eq. (3.12) represent the same quantity – the final angle of each sub-division. A simple rearrangement of this equation then yields:

$$N = \frac{j2\pi}{\alpha}. \quad (3.13)$$

Since each reflection may only increase the number of sub-divisions in multiples of two, we deduce that N must be an even number. The positive integer j now appears to take on the meaning of the number of complete cycles required to return the apexes back onto one another. At present we cannot offer a simple analytical method of determining j , but can offer the following conditions: (i) j is the lowest positive integer such that N is even, and (ii) $j \leq i$. Eqs. (3.11) and (3.13) are predictions as to which initial angles α will result in stable petal pattern output, and how many petals will be observed in the pattern respectively. A plot of the allowed angles for petal pattern formation together with the number of petals that will be observed is shown in Fig. 3.5.

Since the sub-divisions divide the circle finitely, the angle subtended by each sub-division is given by:

$$\psi = \frac{2\pi}{N} = \frac{\alpha}{j}. \quad (3.14)$$

Thus the more complete rotations needed to complete the pattern, the smaller the angle of each sub-division. The simplest case is when $i = 1$; then $j = 1$ and the circle is divided into divisions of α . For higher j values the lossless regions between the high loss sub-division lines become small. Thus although there is an infinite number of solutions for α that lead to finite sub-divisions of the field, if the number of divisions is too large, diffraction will blur the spot structure and no petal pattern will be observed.

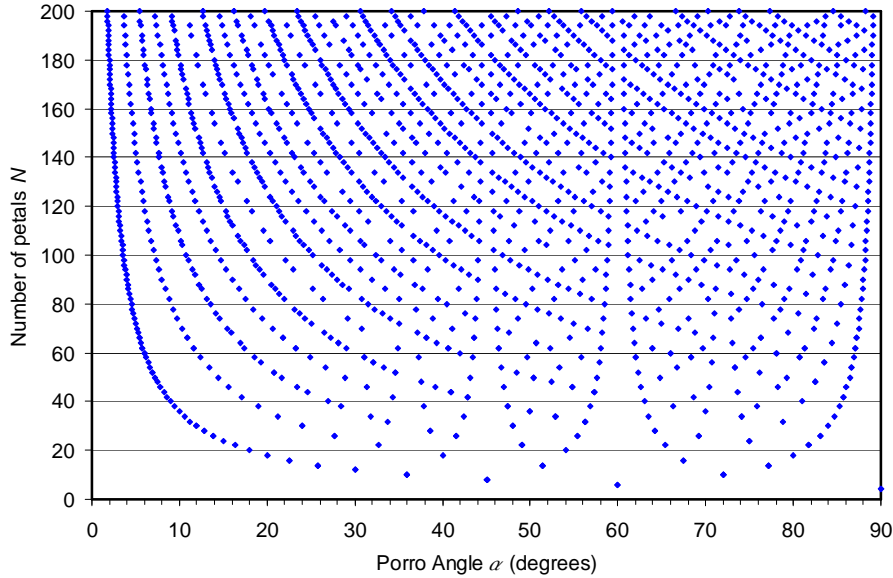


Fig. 3.5. Plot of the discrete set of angles α that give rise to a petal pattern, with the corresponding number of petals to be observed. Data calculated for $m \in [1,100]$ and $i \in [1,50]$.

Taking this into account, and considering the diffraction of a field propagating between areas of high losses, it is reasonable to suppose that the approach and theory presented here is the explanation for the observed (and sometimes not observed) petal patterns from Porro prism resonators. The governing equations for the onset of petal patterns and the number of petals observed are given by Eq. (3.11) and Eq. (3.13) respectively.

3.3 Test resonator

The Porro prism resonator investigated in this study is shown schematically in Fig. 3.1, and was based on a flash lamp pumped Nd:YAG laser with passive Q-switching. The active medium was a 50 mm long Nd:YAG rod of radius 3 mm. Two Porro prisms at either end of the laser formed the resonator, replacing traditional mirrors. The stability of the resonator was determined by the two intra-cavity lenses near the prisms, but in our experiment as well as in the numerical model no intracavity lenses were used, yielding a marginally stable resonator. The resonator was confined in the transverse direction by the clear aperture of the optical elements, such as lenses, prisms and gain rod, but also by inserted apertures not shown in the figure. The laser was pulsed using a Cr^{4+} :YAG passive Q-switch. A quarter-wave plate together with a polarizing

beamsplitter cube ensured variable output coupling from the laser by polarization control (by rotation of the waveplate or by rotation of the prisms).

3.3.1 Experimental set-up

The assembled laser used in our experiments is shown in Fig. 3.6. The spatial intensity profile of the laser output was measured using a CCD camera (model COHU 4812). The temporal characteristics were detected with a silicon detector coupled to a 50Ω impedance, and displayed on a two channel oscilloscope (Tektronic TDS 360).

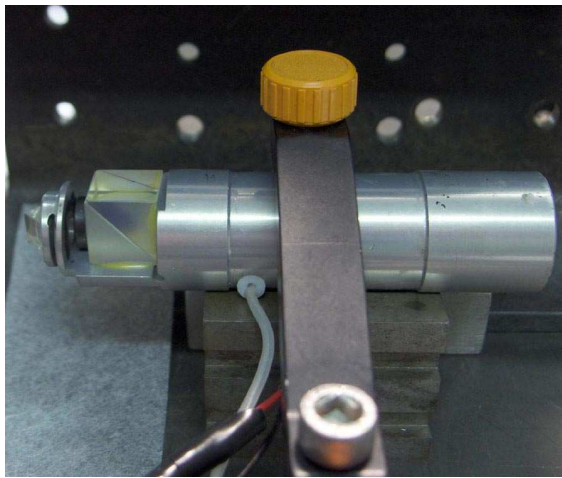


Fig. 3.6. Photograph of assembled laser. The beamsplitter cube and one of the Porro prisms can be made out on the left of the assembly.

3.3.2 Numerical modeling

The laser was modeled as the complete resonator sans any gain, using the Prony method [3.10]. A beam array size of 1024×1024 was used, and the modal build-up modeled until the losses per round trip stabilized to within 0.5%. The Porro prism resonator was modeled by successive passes through a folded-out resonator using the approach described in Section (3.2). Each prism was assumed to be equivalent to a perfect mirror superimposed on a rotating loss line (see Fig. 3.2), with the rotation of the loss region for prism 1 given by Eq. (3.3) and that for prism 2 by Eq. (3.6).

3.4 Results and discussion

Using Eqs. (3.11) and (3.13), the finite sub-division of the field is predicted at angles $\alpha = 67.5^\circ$ and $\alpha = 77.14^\circ$, with associated petal numbers of 10 and 14 respectively. No finite sub-division is expected at $\alpha = 79.0^\circ$. These cases are shown in Figs. 3.7 (a) – (c) respectively, where the locations of the prism apexes are shown around the unit circle after several hundred rotations. In insets (a) and (b) the apexes are clearly repeating on themselves, resulting in a stable pattern, whereas in (c) the field does not result in any lossless regions because of the non-repeating apex positions. This latter situation prohibits the formation of a stable mode since all regions have high loss, while the former scenarios could potentially support lasing in the lower loss regions of the field.

The numerical model of the resonator confirms this (see Figs. 3.7 (d) – (f)), showing a stable mode pattern for $\alpha = 67.5^\circ$ and $\alpha = 77.14^\circ$, with the correct number of petals (10 and 14 respectively) as predicted by the theory. At $\alpha = 79.0^\circ$ the output mode never stabilizes and results in a random field with high losses. Experimental results verify these findings, with petal patterns occurring when they should ($\alpha = 67.5^\circ$ and $\alpha = 77.14^\circ$), and with the correct number of petals: 10 and 14 respectively (see Fig. 3.7 (g) and (h)). At $\alpha = 79.0^\circ$ no petal pattern was observed experimentally, in agreement with the theory and numerical model, with the camera image showing the time averaged intensity from the laser. Thus the theoretical, numerical and experimental results are all in very good agreement.

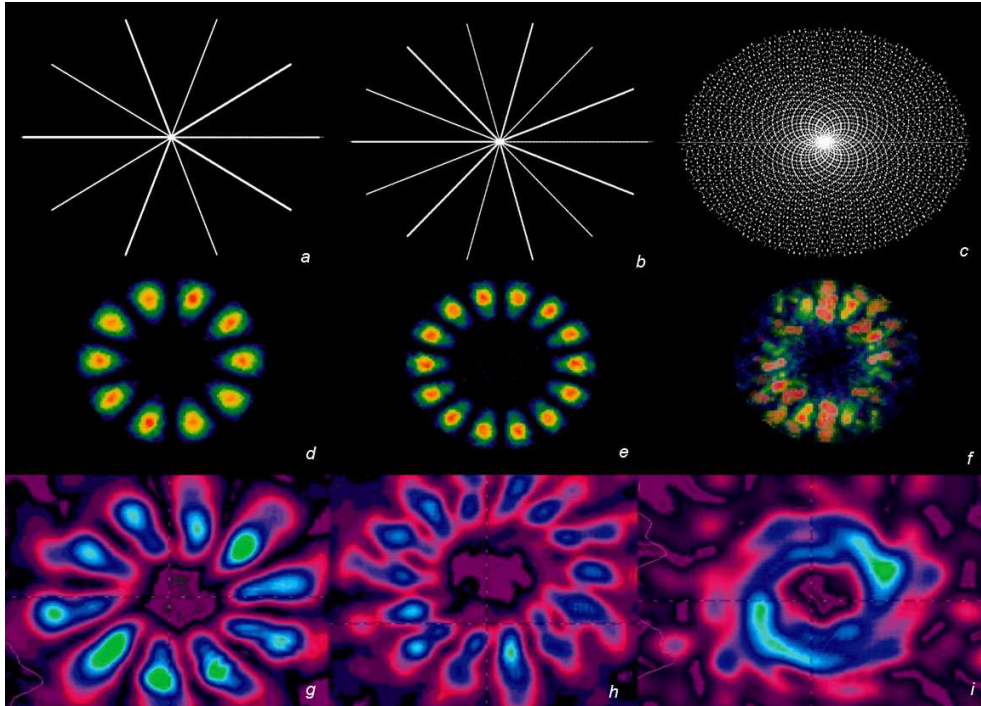


Fig. 3.7. The analytical model depiction of finitely sub-divided fields in (a) and (b), and an infinitely sub-divided field in (c). Numerically this results in a pattern with (d) 10 petals, (e) 14 petals and (f) no petals. The corresponding experimentally observed output is shown in (g) – (i).

The angles α for which an output beam existed for the test laser were limited to between 63° and 87° . The absence of output below 63° was due to increased misalignment between the Porro prisms with decreasing angle away from 90° (the crossed case). It should be noted that this was a particular artifact of the resonator under study, and is not a general property of Porro resonators. The absence of output above 87° was due to two effects: (i) the output coupling method of the given cavity: at 90° (crossed Porro prisms) no output existed because cavity losses were 100% due to the polarization based output coupling method; and (ii) near 90° the number of predicted petals increases very rapidly with Porro angle. Since this reduces the available low loss area for the each petal, either no petals are observed due to the inherently high losses, or the close proximity of the petals leads to blurring due to diffraction.

The available experimental data at selected angles α is shown in Table 3.1, and is in excellent agreement with the theoretical and numerical predictions.

| Experiment | | Theory | |
|--------------------------|-----|-----------------|-----|
| α | N | α | N |
| $68^\circ \pm 0.5^\circ$ | 16 | 67.5000° | 16 |
| $72^\circ \pm 0.5^\circ$ | 10 | 72.0000° | 10 |
| $77^\circ \pm 0.5^\circ$ | 14 | 77.1429° | 14 |
| $80^\circ \pm 0.5^\circ$ | 18 | 80.0000° | 18 |

Table 3.1. Petal pattern observations: theory and experiment

In addition to the experimentally verified petals, the numerical model was used for extensive tests on the analytical predictions of Section (2). Fig. 3.9 shows examples of some results, with the analytical prediction of the stabilized sub-division of the field shown in the top row, with corresponding petal patterns calculated numerically shown below. The top row of Fig. 3.8 shows the calculated apex positions after rotation by Eqs. (3.4) and (3.7), after a stable pattern has emerged. The model correctly predicts all the salient features of the petal pattern.

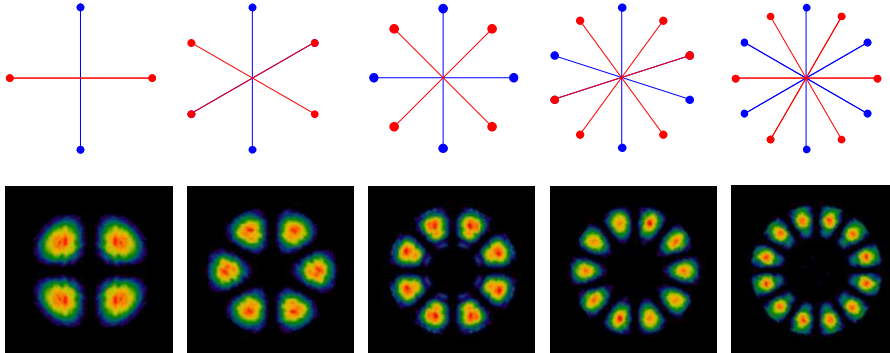


Fig. 3.8. Analytically calculated sub-division of the field using Eqs. (3.4) and (3.7) (top row), with corresponding petal patterns calculated numerically using this model.

Associated with an increase in the sub-division of the field is an increase in the loss per round trip inside the laser cavity.

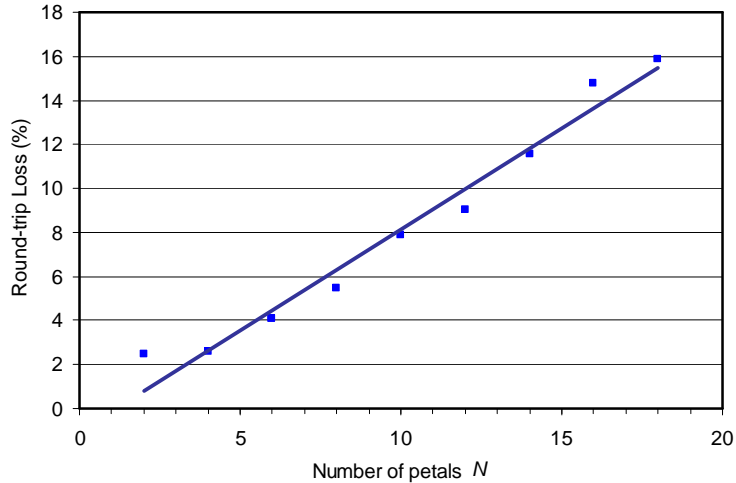


Fig. 3.9. Plot of the round-trip loss as a function of the number of petals as predicted by the numerical model.

Fig. 3.9 shows that the stabilized round-trip losses increase nearly linearly with the number of petals in the petal pattern over the region that one might reasonably expect to observe petals. This is due to the ever decreasing low loss area as the sub-divisions become closer together. This places restrictions on the allowed Porro angles can actually be observed experimentally from such lasers.

3.5 Conclusion

We have presented a new approach to modeling Porro prism resonators that combines geometrical and physical optical aspects. We have shown why such resonators must sometimes generate petal-like patterns, and given the generating equation for the prism angles at which this will happen. The results are confirmed experimentally on a test resonator. Variable output coupling based on rotating the prisms is often employed, but as has been shown here, this will have a significant impact on the output mode from the laser, affecting laser beam propagation, far field laser intensity and laser brightness.

Appendix (Double pulse)

By serendipity we noticed that in some experiments a second pulse of energy delayed in time was observed, occurring roughly 25 μs after the first pulse. Further investigation revealed that the occurrence of the second pulse was

always associated with a change in the spatial intensity pattern from the resonator. It was found that the observation of the second pulse was a function of the gain of the laser: below a threshold pump level no double pulse was observed, while above the threshold two pulses were consistently evident. The single pulse intensity profile fits well with the petal model previously described, while the two-pulse time averaged intensity profile is similar to that predicted, but with an additional ring-like structure in the centre of the pattern (see Fig. 3.10).

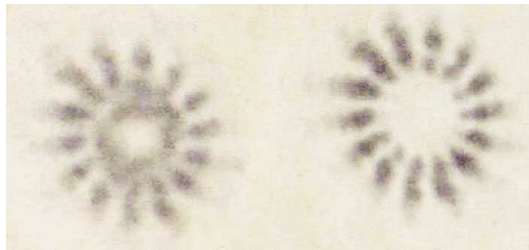


Fig. 3.10. The transverse field distribution, with (a) two and (b) one pulse. The angle between the Porro prisms is 13 degrees (giving 14 spots).

We suggest that this additional feature in the double-pulse intensity profile can be explained by the fact that the first petal-like pulse leaves a region of excess gain in the centre of the Nd:YAG rod, allowing lasing to continue for modes with much higher losses, hence the delay in output. The continuous band may be due to diffractive smearing of the very close petals. It also hints at the possibility of perhaps more complex modes that can oscillate inside such resonators.

Chapter 4

Bessel–Gauss resonator with internal amplitude filter

In this Chapter we present a combination of both amplitude and phase beam shaping inside a cavity, namely the deployment of a suitable amplitude filter at the Fourier plane of a conventional resonator configuration with only spherical curvature optical elements, for the generation of Bessel–Gauss beams as the output. For this type of resonator, both the correct selection of amplitude filter size and radius of curvature of the mirror affect the resulting output beam profile. We analyse the loss behavior of the odd and even modes, and show that the lowest order Bessel–Gauss mode does not necessarily have the lowest loss.

4.1 Introduction

Bessel beams (BBs) represent a class of so-called diffraction free solutions to the Helmholtz equation, and have been studied extensively since the seminal work of Durnin *et al.* in the late 1980s [4.1–4.3]. Of more practical relevance are Bessel–Gauss beams (BGBs), which are spatially-infinite BBs confined by a Gaussian envelope in the transverse spatial plane, making them spatially finite. These beams are easily generated external to the laser cavity by illuminating an axicon with a Gaussian beam, and offer a good approximation to the properties of true BBs. A recent review of BBs and BGBs as well as their applications and reconstruction properties can be found in [4.4, 4.5].

Intra-cavity generation of BGBs has been successfully shown through various techniques using non-conventional elements. In [4.6] a new method was proposed for BB generation by means of a confocal resonator with an annular active medium, and an estimation of the size of the “diffraction-free” zone was presented. A proposal is made to apply a Bessel beam to accelerate a beam of

charged particles. Based on the simple interpretation of Bessel beam as a transverse standing wave formed in the interference region between incoming and outgoing conical waves, was proposed in [4.7] an optical resonator that supports modes that are approximations to Bessel-Gauss beams. Axicon-based resonators were independently proposed by Rogel-Salazar *et al.* [4.7] and Khilo *et al.* [4.8]. The axicon-based resonator supporting Bessel modes in [4.8] was composed of two plane mirrors with an axicon placed close to one of them, and it was shown that if the axicon adjacent mirror was concave, then BGBs were produced. Analytical expressions relating parameters of the resonator and characteristics of its modes were obtained and analyzed. The resonator scheme was implemented in an experiment to confirm the possibility of the generation of zero-order Bessel beams. In [4.9] the properties of a Bessel-Gauss resonator design which was proposed in [4.7] was examined, and explained the bell-shaped modulation imposed on its lowest-order mode in terms of an equivalent linear cavity. An unstable cavity was proposed to eliminate this effect, and obtain modes whose intensities resemble a true Bessel function along the diameter of the defining aperture of the resonator. The use of intra-cavity phase conjugating mirrors for BGB generation was shown in [4.10]. More recently axicon-based BGB resonators with concave output couplers were considered [4.11] using both geometrical and wave optics approaches, while unstable axicon-based BB resonators with convex output coupler was presented in [4.12]. In both cases special attention was directed to the dependence of the output transverse profiles, the losses, and the modal frequency changes on the curvature of the output coupler and the cavity length. A simple and compact laser source that directly produces a Bessel-Gauss beam was demonstrated in [4.13]. The laser resonator consists of a diode-end-pumped Nd:YAG crystal, a planar mirror, and a diffractive mirror designed to phase-conjugate only the lowest-order Bessel-Gauss beam.

We present a conventional (i.e., not axicon-based) confocal resonator configuration for the generation of BGBs [4.14]. The mirror parameters are selected so as to form a Fourier transforming pair; when combined with an internal amplitude filter in the form of an annular aperture, the resonator is capable of supporting BGBs of various orders. In such a resonator the Gaussian field enveloping the Bessel field determines the radial modes, while the Bessel

field determines the angular modes. These two functions together give rise to the potential for mode selection based on variable apertures inside the cavity. In Section 4.2 we introduce the resonator concept, and consider an analytical approach to understanding the mode behavior inside the resonator. In Section 4.3 we analyze the resonator using the round trip Fourier transform, and then confirm the findings rigorously using the Fox–Li method in Section 4.4. We comment on the practicality of implementing this concept in Section 4.5.

4.2 Bessel–Gauss Resonator Concept

4.2.1 Bessel–Gauss Beams

An ideal BB of order n can be described by [4.4]:

$$u_{BB}(r, z, \varphi) = A_0 \exp(ik_z z) J_n(k_r r) \exp(in\varphi), \quad (4.1)$$

where J_n is Bessel's function of order n , k_z and k_r are the longitudinal and radial wavevectors with $k = \sqrt{k_r^2 + k_z^2} = 2\pi/\lambda$, with λ the wavelength of the electromagnetic field, and r , z , and φ are the radial, azimuthal and longitudinal co-ordinates respectively. In practice a BB requires an infinite amount of energy to generate, and so Bessel–Gauss Beams (BGBs) are used as an approximation to study the properties of BB over a finite extent.

A BGB is a BB described by Eq. (4.1) but modulated in amplitude by a Gaussian function, and can be expressed at its waist plane as:

$$u_{BGB}(r, \varphi) = A_0 J_n(k_r r) \exp\left(-\frac{r^2}{w_0}\right) \exp(in\varphi), \quad (4.2)$$

where w_0 is the Gaussian $1/e^2$ radius at the waist. After propagating this field a distance z one can easily show that:

$$\begin{aligned} u_{BGB}(r, z, \varphi) = & A_0 \frac{w_0}{w(z)} J_n\left(\frac{k_r r}{1+iz/z_R}\right) \exp\left(-\frac{r^2}{w^2(z)}\right) \\ & \times \exp\left\{-\left[\frac{1}{w^2(z)} - \frac{ik}{2R(z)}\right] \left(r^2 + k_r^2 z^2 / k^2\right)\right\} \exp(in\varphi) \exp(i\phi(z)), \end{aligned} \quad (4.3)$$

where

$\phi(z) = k_r z - \arctan(z/z_R)$ and $R(z) = z[1 + (z_R/z)^2]$ is the radius of curvature of the Gaussian wavefront. The Gaussian $1/e^2$ beam radius at the distance z is described by $w(z) = w_0 \sqrt{1 + (z/z_R)^2}$.

The constant z_R represents the Rayleigh range of the Gaussian field, and is an indication of the distance over which the field may be considered collimated, given by:

$$z_R = \frac{\pi w_0^2}{\lambda}.$$

Eq. (4.3) is valid when the starting BGB has a waist at $z = 0$, i.e., the wavefront is initially flat. It is equally valid to define the propagation of the BGB with a starting wavefront that has some curvature R , for example by replacing Eq. (4.2) by

$$U_{BGB}(r, \varphi) = A_0 J_n(k_r r) \exp\left(-\frac{r^2}{w_0^2}\right) \exp(in\varphi) \exp\left(\frac{-ikr^2}{2R}\right). \quad (4.4)$$

We point this out since the field described by Eq. (4.4) will be shown to be one of the modes of the resonator described in this Chapter and its propagation in the resonator will be studied in detail.

4.2.2. Fourier Transforming Resonator

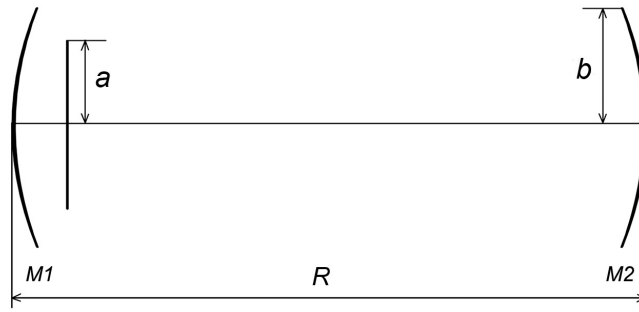


Fig. 4.1. Illustration of the Bessel-Gauss resonator. Mirror M_1 is obscured by a disk of radius a , thereby forming an annular lossless zone in the region $a < r < b$. Each mirror has a radius of curvature of $2f$ and they are separated by a distance of $2f$.

When the geometric parameters of a resonator are chosen appropriately, the spherical curvature mirrors act as a Fourier transforming pair. In particular, if a stable resonator arrangement is employed with two concave mirrors having

radius of curvature equal to the resonator length then the oscillating field will be Fourier transformed after each pass, so that after one complete round trip (two passes) the field is reproduced. The resonator we propose for this purpose has identical end mirrors, each of radius of curvature $R = 2f$, and separated along the optical axis by a distance $L = 2f$. A schematic of this resonator is shown in Fig. 4.1. Both mirrors M_1 and M_2 are of radius b , with M_1 having an additional obscuration in the form of a disk of radius a , creating an annular lossless zone between the disk edge and the mirror edge. The annular lossless zone is a significant factor in this resonator, and deserves further discussion. It has been shown previously [4.10] that when an intra-cavity lens is inserted into a planar-planar resonator such that the opposite mirrors are separated by one focal length from the lens (with the lens in the centre of the cavity), then a Fourier-transform relationship between the modal fields at the mirrors is established. Such a resonator was found to support Bessel–Gauss modes. It was pointed out that the modal discrimination of the resonator would be expected to be poor unless an annular aperture is employed at one of the mirrors. The resonator proposed in this study is analogous to such a cavity, but with spherical mirrors forming a Fourier-transforming pair. We will show in the Sections to follow that the annular aperture size (a) and the mirror size (b) can be used as a mode selector where higher order Bessel fields have lower losses than lower order Bessel fields.

The field at mirror M_1 is uniquely defined by the lossless annular aperture, which if sufficiently narrow ($b - a \rightarrow 0$), will Fourier transform to a Bessel field. Since mirror M_2 is this Fourier transforming plane, the field distribution at M_2 would be the Bessel field. However the resonator we propose also supports Gaussian modes (we assume the dimensions of mirror M_2 are such that higher order Hermite–Gauss modes are eliminated) since the mirror curvatures match the curvature ($R(z)$) of the oscillating Gaussian field. So long as the Gaussian beam width encloses sufficiently many Bessel zeros, a well-defined annulus with an approximately Gaussian radial intensity distribution can be expected at mirror M_1 , in keeping with the concept of Bessel–Gauss fields as a superposition of conventional Gaussian beams with optical axes distributed uniformly on the surface of a cone [4.2]. Note that the resonator parameters

(such as length and mirror curvatures) determine the Gaussian mode that oscillates, defining the radial modes of the resonator, while the apertures inside the resonator determine the angular modes that oscillate, as will be shown later. Both these modes play an important role in the analysis to follow.

4.2.3 Resonant Modes

While the above description also serves as a heuristic argument for BGBs as modes of our resonator, it is instructive to show this more rigorously. We do so in two ways: firstly, we have shown numerically that BGBs of various orders are eigenmodes of this resonator. We pre-empt the discussion later by pointing out that a Fox-Li analysis of this resonator, starting from a random noise field, converges to various BGB orders, depending on the parameters of a and b .

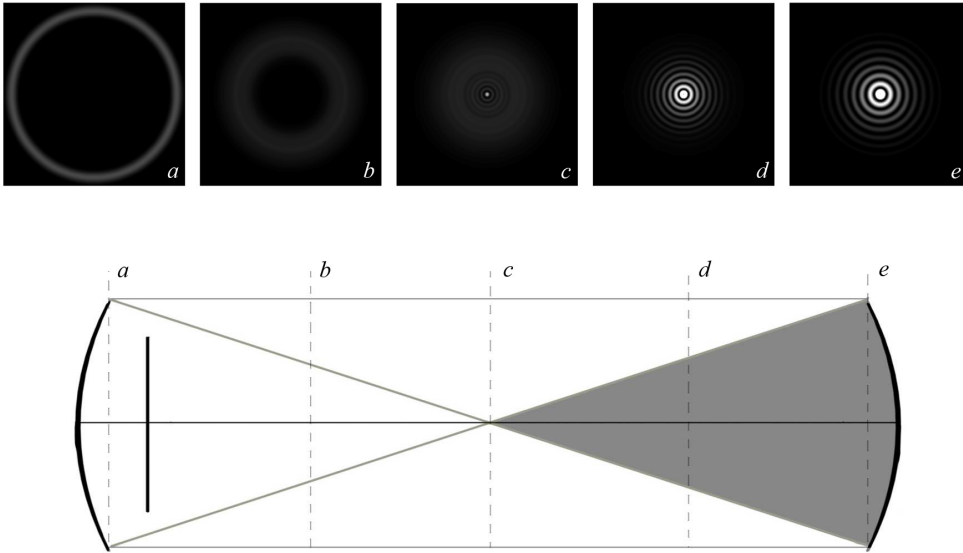


Fig. 4.2. The BGB is formed in the shaded region of the resonator, and changes in intensity as it propagates through this volume. Five intensity plots are shown corresponding to planes (a) through (e) within the resonator for the zeroth Bessel mode ($n = 0$). The starting mode was calculated using the Fox-Li algorithm with ten round trips, Fresnel number $N = 6$ and $a = \frac{5}{6}b$, and then propagated using Eq. (4.6).

Fig. 4.2 shows intensity plots (a – e) of the zeroth order BGB during propagation through the resonator after the mode has reached a steady-state. The shaded area in the resonator drawing indicates the region where the BGB is in existence, with its largest spatial extent at mirror M_2 (position e), finally creating an annular ring at the opposite mirror (position a). This propagation is what is

expected if the mode is a BGB. From the Fox-Li calculations one can also extract the phase of the BGB at the mirror (say mirror M_2 for example). This is shown in Fig. 4.3, where the numerically calculated phase matches that of the mirror's curvature exactly, as expected. Thus we can conclude that the field at mirror M_2 is indeed a BGB, with a wavefront matching the curvature of the mirror, i.e., $R = 2f$.

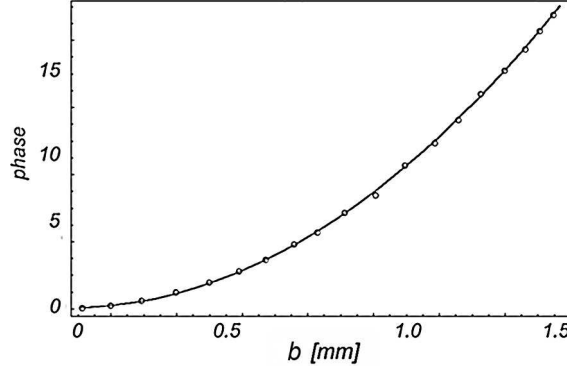


Fig. 4.3. Mirror phase as calculated from Eq. (4.7) (solid curve) as compared to the numerically calculated phase using the Fox-Li algorithm (data points).

Secondly, we follow the approach detailed in [4.10] to test more rigorously if a BGB with a spherical wavefront is an eigenmode of this resonator. We start with a field just prior to reflection off mirror M_2 :

$$u_2(r, \varphi) = A_0 J_n(k_r r) \exp\left(-\frac{r^2}{w_2^2}\right) \exp(in\varphi) \exp\left(\frac{ikr^2}{4f}\right), \quad (4.5)$$

where w_2 is the beam size on mirror M_2 and is given by $w_2 = 3^{-\frac{1}{4}} \sqrt{\frac{8f}{k}}$. If the z axis is defined to be $z = 0$ at mirror M_2 , and positive to the left (in the direction of mirror M_1) then the Gaussian mode will propagate symmetrically about a waist centered at $z_0 = f$ with $w_0 = 3^{\frac{1}{4}} \sqrt{\frac{2f}{k}}$. We can determine the complete propagation of the field u_2 by using the Fresnel diffraction integral in the form [4.13]:

$$\begin{aligned} u(\rho, z) = & -i^{n+1} (k/z) \exp(ikz) \exp\left(\frac{ik}{2z} \rho^2\right) \int_0^\infty u_2(r) J_n\left(\frac{k\rho r}{z}\right) \\ & \times \exp\left(\frac{ik}{2z} r^2\right) \exp\left(-\frac{ik}{2f} r^2\right) r dr, \end{aligned} \quad (4.6)$$

where we have assumed that since the resonator is rotationally symmetric the modes are separable, and where we have made use of the well known integral representation of the Bessel functions:

$$\int_0^{2\pi} \exp(ix \cos \varphi) \exp(in\varphi) d\varphi = i^n 2\pi J_n(x).$$

The kernel of the integral includes phase modulation by mirror M_2 , which we treat as a thin lens of focal length f , followed by free space propagation through a distance z . The field at mirror M_1 will then be given by $u_1(\rho) = u(\rho, 2f)$, thus

$$\begin{aligned} u_1(\rho) &= -i^{n+1} A_0(k/2f) \exp(i2kf) \exp\left(\frac{ik}{4f} \rho^2\right) \int_0^\infty \exp(-(r/w_2)^2) J_n(k_r r) J_n\left(\frac{k\rho r}{2f}\right) \\ &\quad \times \exp\left(\frac{ik}{4f} r^2\right) \exp\left(\frac{ik}{4f} r^2\right) \exp\left(-\frac{ik}{2f} r^2\right) r dr \\ &= -i^{n+1} A_0(k/2f) \exp(i2kf) \exp\left(\frac{ik}{4f} \rho^2\right) \int_0^\infty \exp(-(r/w_2)^2) J_n(k_r r) J_n\left(\frac{k\rho r}{2f}\right) r dr. \end{aligned}$$

By making use of the well known relation:

$$\int_0^\infty \exp(-\sigma^2 x^2) J_p(\alpha x) J_p(\beta x) x dx = \frac{1}{2\sigma^2} \exp\left(-\frac{\alpha^2 + \beta^2}{4\sigma^2}\right) I_p\left(\frac{\alpha\beta}{2\sigma^2}\right),$$

one can easily show that the field at mirror M_1 is given by:

$$\begin{aligned} u_1(\rho) &= -iA_0 \frac{w_2^2}{4f} \exp(i2kf) \exp\left(-\frac{1}{4} w_2^2 \left[k_r^2 + \frac{k^2 \rho^2}{4f^2}\right]\right) \\ &\quad \times J_n\left(\frac{ikk_r w_2^2}{4f} \rho\right) \exp\left(\frac{ik}{4f} \rho^2\right). \end{aligned} \tag{4.7}$$

Now we note that the required transfer function for mirror M_1 to support this mode can be found from:

$$t_{M1} = \frac{u_1^*}{u_1} = \exp\left(-\frac{ik}{2f} \rho^2\right),$$

where we have ignored constant phase terms. But this is precisely the phase of a spherical mirror of radius of curvature $R = 2f$, thus indicating again that the various orders of BGBs are modes of this resonator.

It is worth pointing out here an interesting aspect of this resonator. Conventionally one would consider the Fourier transform plane to be at $z = f$

and not $z = 2f$ when using a mirror of focal length f (or curvature of $2f$). However, the incoming field already has curvature (see Eq. (4.5)), and thus the effective focal length of the mirror to a planar phase BGB field appears as $2f$:

$$\begin{aligned}
 u(r) &= A_0 J_n(k_r r) \underbrace{\exp\left(-\frac{r^2}{w_2^2}\right)}_{\text{BGB}} \underbrace{\exp\left(\frac{ikr^2}{4f}\right)}_{\text{lens } (f)} \underbrace{\exp\left(-\frac{ikr^2}{2f}\right)}_{\text{lens } (f)} \\
 &= A_0 J_n(k_r r) \underbrace{\exp\left(-\frac{r^2}{w_2^2}\right)}_{\text{planar BGB}} \underbrace{\exp\left(-\frac{ikr^2}{2(2f)}\right)}_{\text{lens } (2f)}.
 \end{aligned}$$

It is for this reason that the resonator mirrors are separated by a distance of $2f$.

The intensity profile at mirror M_1 is thus an annular beam modulated by a Gaussian envelope, while the intensity at mirror M_2 is the reconstructed BGB (Fourier transform of the annular field). If mirror M_2 is made partially transmitting, the resonator will emit various orders of Bessel–Gauss modes. Suitable collimating optics may be employed to correct the phase of the output beam if so desired.

4.3 Fourier Optics Analysis

We wish to consider the diffraction losses for each BGB order by applying the Hankel transform in Eq. (4.6) to propagate the field from mirror M_2 to M_1 , but with the limits of integration adjusted to $[0, b]$. The energy of the initial field is normalized such that the diffraction losses for the BGB of order n may be written as $\gamma = 1 - E_n$ where E_n is the energy at mirror M_1 after one pass. This single pass loss is representative of the steady state diffraction loss since the initial field chosen is already close to the stable mode under investigation. Because the field on mirror M_1 is annular–like for all mode numbers, showing very little discrimination between the modes, increasing or decreasing the diaphragm radius a (or the mirror radius itself) will result in either increasing or decreasing losses for every BB order in a concomitant manner. Conversely, the BGB on mirror M_2 varies greatly with the Bessel function order. When the size of mirror M_2 is chosen so that b coincides with an intensity trough of the BGB, the diffractions losses will be minimized. In contrast, when b coincides with an

intensity peak of the BGB, the diffractions losses will be maximized. This is easily noted if one considers that when $k_r r$ is large, Eq. (4.1) may be approximated as:

$$u_{BB}(r, \varphi) = A_0 \sqrt{\frac{2}{\pi k_r r}} \cos\left(k_r r - \frac{2n+1}{4}\pi\right) \exp(in\varphi), \quad (4.8)$$

where we have dropped the piston phase term ($\exp(ik_z z)$). From this asymptotic approximation we observe that the amplitude of the field will oscillate with a cosine function for even orders of n , and as a sine function for odd orders of n , thus the even and odd orders are out of phase. This results in the diffraction losses of the modes on this mirror having an oscillatory character. One can also derive from Eq. (4.8) simple expressions for the radius b at which a particular order will have high or low losses:

$$b_{HL} = \frac{\pi\left(m + \frac{1}{2}n + \frac{1}{4}\right)}{k_r}, \quad (4.9a)$$

$$b_{LL} = \frac{\pi\left(m + \frac{1}{2}n + \frac{3}{4}\right)}{k_r}, \quad (4.9b)$$

where b_{HL} and b_{LL} are the values of b for high and low losses respectively, m is an integer and n is the order of the BGB. For example, assume that an integer $m = m_0$ is chosen such that the J_0 function has high losses. Selecting an integer $m_1 = m_0 - 1$ will then ensure that the J_1 function has lower losses than the J_0 function. In general, if the integers in Eqs. (4.9a) and (4.9b) are chosen such that $m_0 - m_n = \frac{1}{2}(n + 1)$, then the losses in the J_0 will be larger than that of the J_n . Moreover, the decreasing losses for the even modes imply increasing losses for the odd modes, and vice versa. In the limit that the enveloping Gaussian becomes much smaller than the mirror radius b , we expect this oscillatory behaviour to be suppressed by the zero asymptote of the Gaussian function, and at this point the radial modes completely determine the resonator behaviour.

In the analysis to follow the resonator parameters used for all calculations are: $f = 0.35$ m, $\lambda = 532$ nm, and $a = 0.9b$. Where other values have been used in calculations, it is clearly indicated so in the accompanying text.

The oscillatory nature of the diffraction losses for both odd and even modes, as described qualitatively earlier, is shown quantitatively in Fig. 4.4. The convergence of the losses for all orders of odd and even modes when $b \gg w_2$ is

the norm in Fabry–Perot type cavities. The unusual feature of Fig. 4.4 (a), that the losses increase with increasing b , is due to the fact that a is also increasing according to $a = 0.9b$. Since an increase in obscuration at mirror M_1 increases losses for all modes, the net effect is to increase the overall loss for each mode. Increasing b with a fixed in value, as is shown in Fig. 4.4 (c), results in an expected convergence to low loss for all modes. The results in Figs. 4.4 (a) and (c) have been confirmed with a full Fox–Li analysis. Fig. 4.4 (b) shows a zoomed–in section of Fig. 4.4 (a), with the section shown as vertical markers on Fig. 4.4 (a). The vertical cross–section A in Fig. 4.4 (b) indicates a mirror radius at which some odd modes have higher losses than some even modes, while cross–section B shows the opposite. It is evident that at some values of b the lowest order BGB does not have the lowest losses; in general when the even modes have high losses, the odd modes have lower losses.

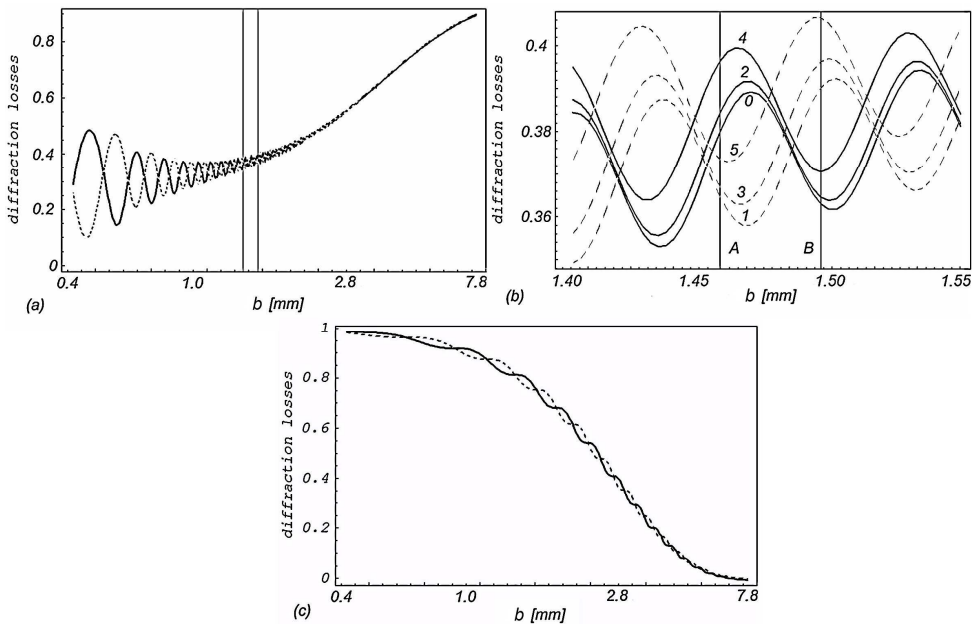


Fig. 4.4. The dependence of diffraction losses on radius b for the various orders of BGBs (even modes as solid curve, odd modes as dashed curve): (a) shows a general trend for the zeroth and first order mode of decreasing oscillation strength with increasing mirror radius due to the Gaussian envelope dominance when $b \gg w_2$. In this plot $a = 0.9b$, and thus the losses increase with b . A zoomed in area (between the vertical solid lines) is shown in (b), with the out of phase oscillations of the odd and even modes evident; (c) shows plot (a) but with a fixed in value.

This fact is illustrated in Fig. 4.5 where it is evident that the BGB of zero order has higher losses than BGBs of order 1, 3, 5 and 7. By judicious selection of b one can again ensure that the zeroth order BGB has the lowest losses, as

shown in Fig. 4.6, where even orders from 0 to 6 have lower losses than the first order BGB.

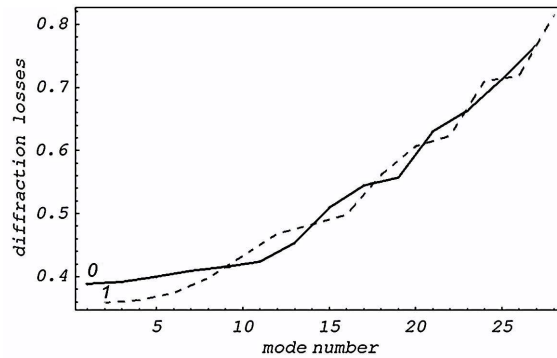


Fig. 4.5. The diffraction losses, as calculated by the Fourier approach, showing the zeroth order mode (0) with higher losses than some odd order modes (shown starting at 1, dashed curve). Calculations done at $b = 1.465$ mm corresponding to cross-section A of Fig. 4.4 (b).

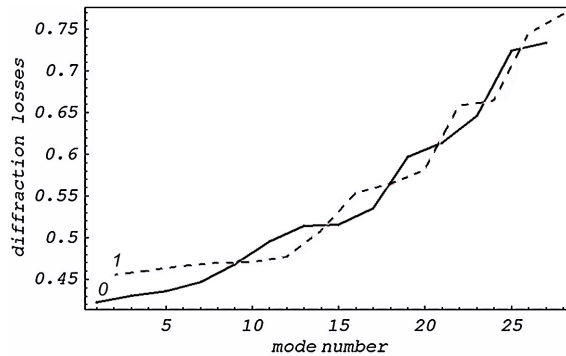


Fig. 4.6. The zero order mode (0) now has the lowest losses, with a clear out-of-phase oscillation in the loss for odd (starting at 1, dashed curve) and even (starting at 0, solid curve) modes. Calculations done at $b = 1.50$ mm corresponding to cross-section B of Fig. 4(b).

We also note from Fig. 4.5 that the oscillatory nature of the mode losses is suppressed at high mode numbers (e.g., beyond 20); this is due to the nature of the oscillations in the Bessel functions themselves, where the approximation (see Eq. (4.8)) becomes valid at radii that increase with the Bessel order.

4.4 Fox-Li Analysis

To confirm the results of Figs. 4.5 and 4.6, we consider a full wave optics analysis using the Fox-Li method [2.2, 5.17]. The calculation was performed with $b = 1.50$ mm and the results are shown in Fig. 4.7. Comparison of Figs. 4.6 and 4.7 clearly shows that the approach of the previous Section is in good agreement with the full wave optics analysis. The oscillatory nature of the losses

for the odd and even orders is evident in both trends, showing excellent qualitative agreement, while there is very close quantitative agreement in the calculated losses.

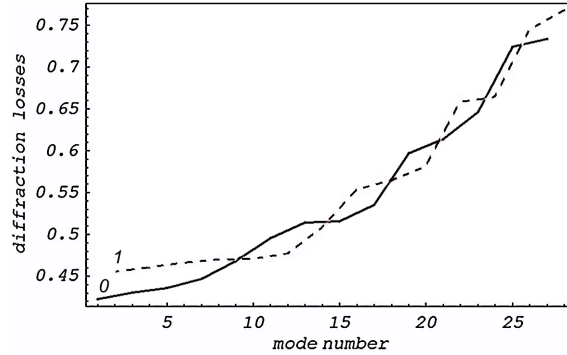


Fig. 4.7. The dependence of the diffraction losses per round trip on the mode number, as calculated using the Fox-Li method. Odd modes are shown starting at 1 in the dashed curve, while even modes are shown starting at 0 in the solid curve. The results are in very good agreement with those shown in Fig. 4.6.

The propagation of the zeroth order BGB is shown in Fig. 4.2, while some examples of the resulting steady state fields and their Fourier transforms are shown in Fig. 4.8. The propagation characteristics, as well as the Fourier transform of the fields confirms that these are indeed BGBs. The fact that the losses for various orders may be to some extent controlled in this resonator opens the way for selection of higher order BGBs.

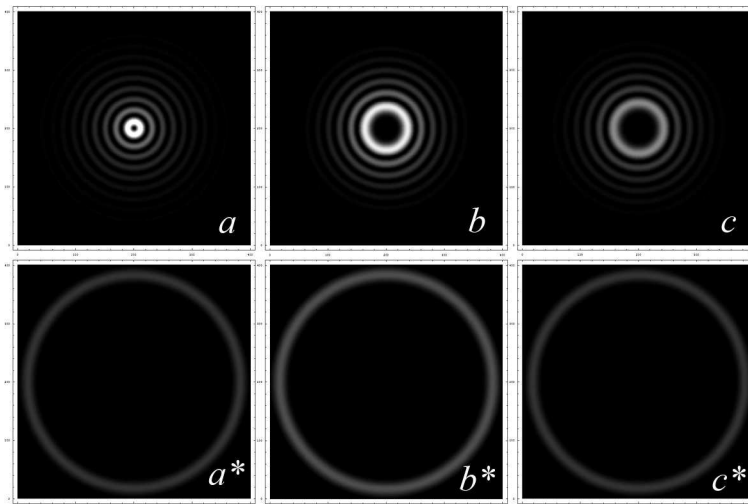


Fig. 4.8. Examples of the calculated BGBs with their corresponding Fourier transforms: (a) J_1 , (b) J_5 and (c) J_6 Bessel orders.

4.5 Conclusion

We have analysed a Fourier transforming type resonator that generates BGBs of various orders as an output. The losses of these modes have revealed an oscillatory nature, which suggests that the lowest order BGB may not necessarily have the lowest loss. This can be understood in terms of odd and even modes by using the asymptotic approximation to the Bessel function. The analytical theory indicates that specific resonator conditions would be necessary to ensure that the lowest loss can be obtained in the lowest order mode. The general rule for Fabry-Perot type resonators, which explains that the lower order modes have lower loss is not necessarily correct in this particular resonator. The simplified Fourier approach was validated by a more rigorous Fox-Li analysis which confirmed the findings.

We also wish to point out some practical implications in generating BGBs from such a resonator. Firstly, since the resonator consists of only conventional optical elements (spherical curvature mirrors and circular apertures) no special alignment techniques are required. Secondly, due to the fact that the order of the BGB of lowest loss is determined only by the diameter of mirror M_2 , a simple variable aperture (iris) at the position of mirror M_2 should suffice as a mode selector in much the same way that the various Hermite-Gauss modes may be selected by suitable aperture choice. This paper has dealt mostly with loss aspects of the modes, but the issue of optical gain requires a mention. As illustrated in Fig. 4.2, the BGB does not fill the entire cavity, and is most pronounced near mirror M_2 . This suggests that the gain medium in a practical system would have to be placed near mirror M_2 and have a larger cross-sectional area and a comparatively short length. For example, if the laser had a solid state gain medium, there would be benefit in using a disk-like gain medium rather than a rod in order to maximize the mode volume inside the gain region. It would also be possible to amplify the field near mirror M_1 , but this would require an annular gain region, which while not impossible, may not be easily implemented in practice.

Finally, the typical aperture dimensions found in this study would not deter practical implementation of such a resonator concept.

Chapter 5

Intra-cavity flat-top beam generation

In this Chapter we present the analytical and numerical analyses of two new resonator systems for generating flat-top-like beams. In both cases we have used phase only intra-cavity beam shaping techniques namely determination (both analytically and numerically) of phase only transformation element(s) which installed into flat-flat mirrors resonator is (are) able to modify the transversal intensity distribution of the fundamental mode into a flat-top with the required propagation properties. Both approaches lead to closed form expressions for the required cavity optics, but differ substantially in the design technique, with the first based on reverse propagation of a flattened Gaussian beam, and the second a metamorphosis of a Gaussian into a flat-top beam. We show that both have good convergence properties, and result in the desired stable mode.

5.1 Introduction

There are many applications where a laser beam with an intensity profile that is as flat as possible is desirable, particularly in laser materials processing. The methods of producing such flat-top beams (FTBs) can be divided into two classes, namely extra- and intra-cavity beam shaping. Extra-cavity (external) beam shaping can be achieved by manipulating the output beam from a laser with suitably chosen amplitude and/or phase elements, and has been extensively reviewed to date [5.1]. Unfortunately amplitude beam shaping results in unavoidable losses, while reshaping the beam by phase-only elements suffers from sensitivity to environmental perturbations, and is very dependent on the incoming field parameters. The second method of producing such beam

intensity profiles, intra-cavity beam shaping, is based on generating a FTB directly as the cavity output mode. There are obvious advantages to this, not the least of which is the potential for higher energy extraction from the laser due to a larger mode volume, as well as an output field that can be changed in size by conventional imaging without the need for special optics in the delivery path. Unfortunately such laser beams are not solutions to the eigenmode equations of laser resonators with spherical curvature mirrors, and thus cannot be achieved (at least not as a single mode) from conventional resonator designs.

The key problem is how to calculate the required non-spherical curvature mirrors of the resonator in order to obtain a desired output field. One method to do this is to reverse propagate the desired field at the output coupler side of the resonator to the opposite mirror, and then calculate a suitable mirror surface that will create a conjugate field to propagate back. This will ensure that the desired field is resonant. This method was first proposed by Belanger and Pare [5.2–5.4], and we will refer to it as the *reverse propagation technique*. It was shown that the intra-cavity element could be defined such that a particular field distribution would be the lowest loss mode, opening the way to intra-cavity beam shaping by so-called graded-phase mirrors. In [5.3] a simple algorithm for designing a stable grade – phase mirror resonator was derived. First, the desired output beam profile of the fundamental mode is propagated into the laser medium. The wavefront is then extracted and serves to determine the appropriate phase profile of the mirror. The diffraction analysis of the resonator using this grade – phase mirror indicates a very low loss for the fundamental mode with a very large discrimination of higher modes. Practical design parameters such as the geometric factor, the Fresnel numbers, and phase profile perturbations are discussed. The authors conclude that this type of resonator can significantly increase the mode volume and favour the single – mode operation of laser systems relying on stable resonator geometry. This principle has been applied to solid state lasers [5.5] namely a diffractive laser cavity is described that can customize the amplitude and phase of a laser mode. The design of this diffractive element is shown for a square, flat – topped fundamental mode. The laser cavity has a theoretical fundamental mode loss of 0.08 % and a second order mode loss of 48.2%, resulting in high modal discrimination. The fabricated mirror is tested in Nd:YAG laser system. In [5.6] the result of [5.5]

was extended by inclusion of an additional internal phase plate for improving the discrimination of undesired higher order modes. However, in general this approach does not lead to closed form solutions for the required mirror phases.

In this Chapter we report on two resonator systems for producing flat-top beams, and show that in both cases closed form expressions may be found for the mirror surfaces [5.15]. We outline a new method for generating a flat-top beam as the output mode of an optical resonator, based on an adaption of well-known external laser beam shaping techniques. This is the first time such techniques have been employed inside a laser resonator. A major advantage of this approach is that simple expressions can be obtained for the mirror surfaces. This approach is compared to the reverse propagating technique for calculating suitable graded-phase mirrors, and is shown to have faster convergence to the fundamental flat-top beam mode, albeit with higher losses. Moreover, we show that by employing an approximation to flat-top beams in the form of Flattened Gaussian Beams (defined later), a closed form solution can be obtained for the mirror surface profiles even in the reverse propagating technique.

Throughout this Chapter a concept resonator with the following parameters is used to illustrate the two approaches to flat-top generation: wavelength of $\lambda = 1064$ nm; optical path length between the mirrors of $L = 300$ mm and an output flat-top beam of width $w_{FTB} = 1$ mm. These parameters have been chosen by way of example only, but can be considered realistic for experimental verification. The round trip modal build up and losses were studied numerically using the Fox-Li approach [2.2], by applying a fast matrix method (see sec. 2) to simplify the calculations and improve accuracy for an allowable computation time.

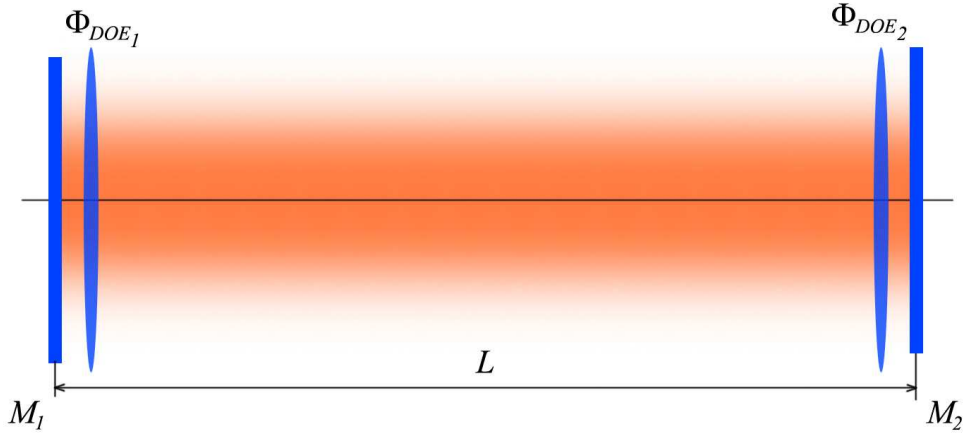


Fig. 5.1. A schematic of the resonator to be modeled: with output coupling at M_2 . Mirrors M_1 and M_2 can either be considered as elements with non-spherical curvature, or as depicted above, as flat mirrors with an appropriate transmission DOE placed immediately in front of each.

The theory outlined in this Chapter, as well as the numerical simulations thereof, are restricted to the problem of one dimensional laser beam shaping, simply to keep the mathematical analysis as simple as possible. The two dimensional beam shaping problem has the same conceptual base, and all the results here may readily be extended to additional dimensions.

5.2 Reverse propagation technique

For the benefit of the reader we briefly outline the reverse propagation technique, first proposed by Belanger and Pare [5.2, 5.3], since it will be used as a point of comparison for a new method proposed later in this paper.

Consider some arbitrary field that may be written in the form:

$$u(x) = \psi(x) \exp[-ik\phi(x)], \quad (5.1)$$

where $k = 2\pi/\lambda$ is the wavenumber, λ is the wavelength, and $\psi(x)$ and $\phi(x)$ are the amplitude and phase of the electric field respectively. The action of a DOE in the form of a phase-only mirror (graded-phase mirror) is to transform the phase $\phi_{in}(x)$ of an incoming field to a new phase $\phi_{out}(x)$ of an outgoing field according to:

$$\phi_{out}(x) = \phi_{in}(x) - 2\phi_{DOE}(x), \quad (5.2)$$

The salient point here is that this transformation takes place in a lossless manner, i.e., the amplitude is unchanged, $\psi_{in}(x) = \psi_{out}(x)$. In particular, one can show [5.2] that if the phase mirror is not spherical, then the change in the mean radius of curvature of the wavefront also depends on the incoming field distribution, $\psi_{in}(x)$. Thus it is expected that such a phase-only mirror will discriminate against those modes that do not have the correct distribution $\psi_{in}(x)$. By invoking the requirement that the mode must reproduce itself after one round trip, and considering the impact of the graded-phase mirror on the curvature of the wavefront, it has been shown that the resulting restriction on the phase of the DOE mirror is given by [5.2]:

$$\int_{-\infty}^{\infty} x \left(\frac{\partial \phi_{in}}{\partial x} \right) \psi_{in}^2(x) dx = \int_{-\infty}^{\infty} x \left(\frac{\partial \phi_{DOE}}{\partial x} \right) \psi_{in}^2(x) dx \quad (5.3)$$

from which we conclude that the phase of the resonator eigenmode is the same as the phase of the DOE mirror, apart from a constant:

$$\phi_{DOE}(x) = \phi_{in}(x) - \phi_{in}(0). \quad (5.4)$$

Combining Eqs. (5.2) and (5.4), and ignoring the constant phase offset, we see that

$$\phi_{out}(x) = -\phi_{in}(x). \quad (5.5)$$

Therefore the reflected beam $u_{out}(x)$ is the phase-conjugate of the incoming beam, $u_{out}(x) = u_{in}^*(x)$. In this resonator only a particular beam distribution is phase conjugated by the DOE mirror, so that the eigenmode of the resonator satisfies the criteria that its wavefront matches the phase of each mirror in the cavity.

If we describe the desired field at the output coupler end (mirror M_2) as u_2 , then reverse propagating the field to the DOE mirror (M_1) using the Huygen's integral in the Kirchhoff-Fresnel approximation yields the field at mirror M_1 as

$$u_1(x_1, L) = \sqrt{\frac{i}{\lambda L}} \int_{-\infty}^{\infty} u_2(x_2) \exp\left(-\frac{i\pi}{\lambda L} (x_1^2 - 2x_1x_2 + x_2^2)\right) dx_2, \quad (5.6)$$

where L is the optical path length of the resonator. If after reflection off mirror M_1 the field u_1 is to reproduce u_2 at the output coupler, then the required phase for the DOE at mirror M_1 must be given by

$$\phi_{DOE_1} = \text{Arg}[u_1^*(x, L)]. \quad (5.7)$$

One can also argue heuristically and reach the same conclusion as follows: one of the main properties of a fundamental mode of optical resonator is that the path of propagation both in the forward and in the reverse direction must repeat on one another. Consequently, in order to obtain a fundamental mode of a desired intensity profile we have to find a way to force the electromagnetic wave to follow exactly the same path in the forward and the reverse propagation directions. The conjugate of an incoming wave will produce an outgoing wave with exactly this property. Consequently we require that:

$$\exp(i\phi_{out}(x)) = \exp(-i\phi_{in}(x)) = \exp(-i2\phi_{DOE}(x))\exp(i\phi_{in}(x)), \quad (5.8a)$$

and hence

$$\phi_{DOE}(x) = \phi_{in}(x), \quad (5.8b)$$

which is consistent with Eqs. (5.4) and (5.5). This is the basis by which custom resonators may be designed. In the following Section we outline how this method may be applied to the generation of flat-top-like beams.

5.3 Flattened Gaussian Beam resonator

The limitation in the approach outlined above is that the required mirror surface, as given by Eq. (5.7), is the solution to an integral problem Eq. (5.6) for which there is often not a closed form expression. Here we outline a suitable approximation to flat-top beams that leads to an analytical expression for the mirror surface.

5.3.1 Flattened Gaussian Beams

The exact definition of a flat-top beam (FTB) is one with constant field amplitude in some well defined region, and zero amplitude elsewhere:

$$u_{FTB}(x) = \begin{cases} u_0, & |x| < w \\ 0, & |x| \geq w \end{cases}, \quad (5.9)$$

where w is the radial width of the beam, and u_0 is a constant. Such a field does not result in a closed form solution to the problem of how the field appears after propagation through some distance z . However, there are many classes of flat-top-like beams that exhibit very similar propagation properties to true flat-top beams, where the rate of divergence (and profile shape change) may be controlled by a scale parameter closely coupled to the steepness of the edges and the flatness of the intensity profile at the centre of the beam [5.7]. Such classes of beams have been extensively studied both theoretical and experimentally [5.7–5.10]. One such class is the so-called Flattened Gaussian Beam (FGB), with a field distribution given by [5.10]:

$$\begin{aligned}
 u_{FGB}(x, z) = & \sqrt{\frac{ik}{2z}} \exp\left[-\frac{ikz}{2}\right] \exp\left[-\frac{ikx^2}{2z}\right] \exp\left[-\frac{\left(\frac{kx}{z}\right)^2}{4\left(\frac{N+1}{w^2} + \frac{ik}{2z}\right)}\right] \\
 & \times \sum_{m=0}^N \left(\frac{1}{4}\right)^m \frac{1}{m!} \left(\frac{N+1}{w^2}\right)^m \left(\frac{N+1}{w^2} + \frac{ik}{2z}\right)^{-m} H_{2m}\left(\frac{\frac{kx}{z}}{2\sqrt{\frac{N+1}{w^2} + \frac{ik}{2z}}}\right),
 \end{aligned} \tag{5.10}$$

where H_{2m} is the Hermite polynomial of order $2m$, and all other terms have their usual meaning. Such a field represents a suitably weighted linear combination of Hermite modes, such that the resulting intensity approximates a flat-top beam. The linear combination of fields with known propagation properties in turn allows the resulting field's propagation characteristics to be known analytically too, such as Rayleigh range, beam quality factor etc. The advantage of this profile as an approximation to a flat-top beam over that of others is that Eq. (5.10) offers an analytical expression for its profile at any propagation distance z . The 'scale parameter' associated with the field, given by the summation index N , allows the approximation to true flat-top beams to be exact when $N \rightarrow \infty$. In general as the scale parameter increases, so the effective Rayleigh range decreases and the beam quality factor increases, resulting in a rapidly changing profile during free space propagation.

To design a resonator for such a beam, one simply follows the procedure outlined in Section 2:

1. Select the desired field at the output coupler as $u_2 \equiv u_{FGB}(x, 0)$;
2. Reverse propagate this field using Eq. (5.10) to find the field at the opposite mirror, $u_1 = u_{FGB}(x, L)$;
3. The desired phase of the DOE at mirror M_1 is then given by

$$\phi_{DOE_1} = \text{Arg}[u_1^*].$$

This approach may be used to calculate a suitable intra-cavity DOE that generates a FGB approximation to a flat-top beam as the resonant mode of the cavity. Following this procedure, we calculated the required mirror surface, shown in Fig. 5.2, to generate an $N = 20$ FGB, with $w_{FGB} = 1$ mm, as the output mode of the cavity. Since we wish the wavefront to be planar at the output coupler side, mirror M_1 has a planar surface.

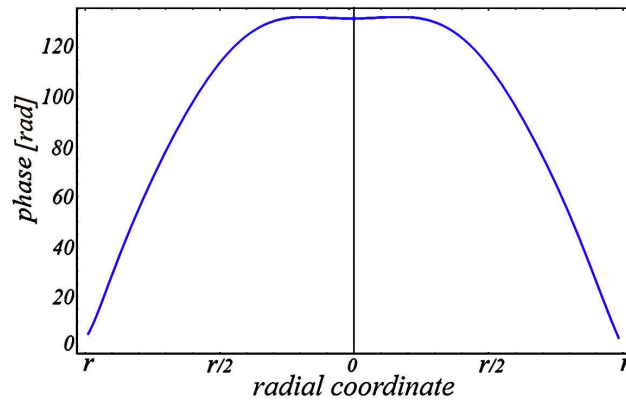


Fig. 5.2. Calculated phase profile required for the DOE at mirror M_1 . The requirement for the DOE at M_2 is that it is a planar surface.

The resulting analysis of such a resonator is shown in the next Section.

5.3.2 Simulation results

The calculated beam intensities at each mirror, for an $N = 20$ FGB, with $w_{FGB} = 1$ mm, are shown in Fig. 5.3 (a), together with the phase of the field at each mirror in Fig. 5.3 (b). The simulated results represented the field after stability using the Fox-Li approach, starting from random noise. The choice of $N = 20$ ensures a good quality flat-top beam, with reasonable Rayleigh length – i.e., the field does not change shape appreciably on propagating across the resonator length $L = 300$ mm (Fresnel number of ~ 50).

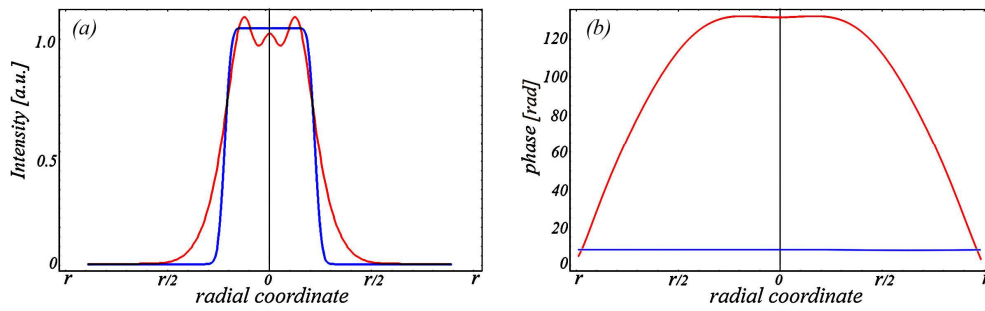


Fig. 5.3. The simulated field at mirror M_1 (red) and M_2 (blue): (a) intensity, showing a near perfect flat-top beam at M_2 , with slight change in flatness after propagating across the resonator to M_1 , (b) phase of the field, with a flat wavefront at M_2 as anticipated from the design.

It is clear that the approach outlined above correctly produces the desired FGB as the output mode of the resonator.

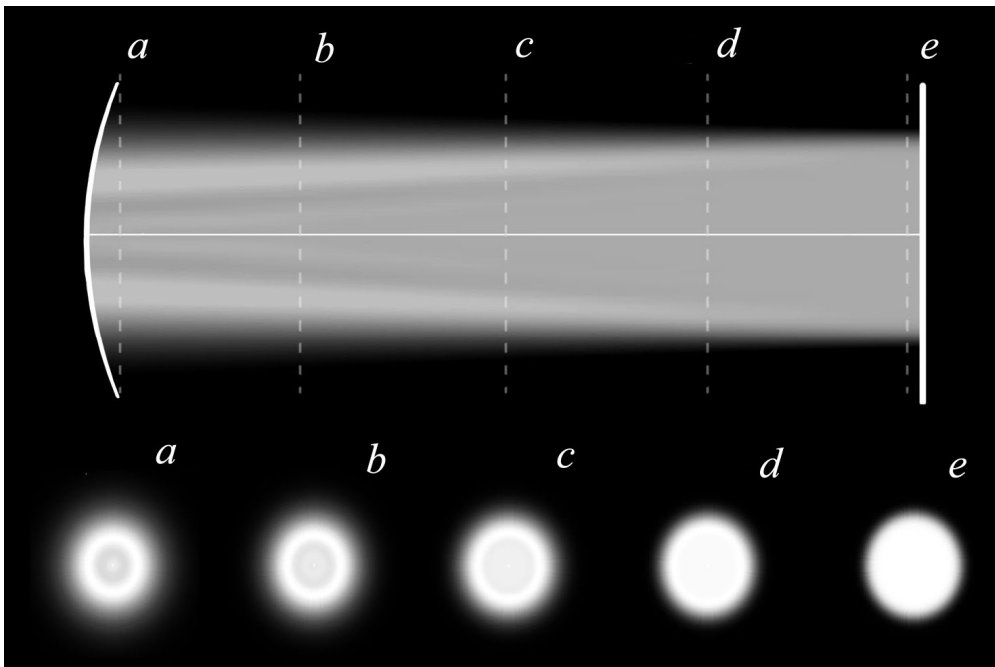


Fig. 5.4. The simulated field as it propagates across the resonator after stabilization, from M_1 (left) to M_2 (right). The perfect flat-top beam develops some intensity ‘structure’ as it propagates away from M_2 . This is in accordance with the propagation properties of such fields, and may be minimized by suitable choice of Rayleigh range of the field.

A cross-section through the resonator of the stabilised field is shown in Fig. 5.4, together with density plots of the field intensity at various planes in the resonator. The advantage of this order of FGB is that the beam is very close to an ideal flat-top, but with little change in the beam’s cross-sectional intensity during propagation (in the absence of gain) across the resonator.

5.4 Flat-top resonator

Here we outline a new method for generating flat-top beams inside a laser resonator, based on an external lossless beam shaping technique converting a Gaussian input field to a flat-top output field [5.11, 5.12]. To the best of our knowledge these techniques have not been previously adapted or exploited for intra-cavity laser beam shaping.

5.4.1 Theory

Since we have *a priori* knowledge of how this resonator will be realised, consider a Gaussian field at mirror M_1 of the form $u_1(x) = \exp(-(x/w_g)^2)$, where w_g is the radius of the field at $1/e$ of its peak value. If the DOE at mirror M_1 is made up of a Fourier transforming lens and a transmission phase-only element, ϕ_{SF} , and the resonator length is selected to match the focal length of the Fourier transforming lens ($L = f$), then the resulting field at mirror M_2 will be given by:

$$u_2(x_2, f) = \sqrt{\frac{i}{\lambda f}} \int_{-\infty}^{\infty} u_1(x_1) \exp\left[-i\left(\phi_{SF}(x_1) - \frac{ikx_1^2}{2f}\right)\right] \times \exp\left(-\frac{i\pi}{\lambda f}(x_1^2 - 2x_1x_2 + x_2^2)\right) dx_1. \quad (5.11)$$

We may apply the method of stationary phase to find an analytical solution for the phase function ϕ_{SF} , such that the field u_2 is a perfect flat-top beam, of width w_{FTB} . It has been shown that this may be expressed as [5.11]:

$$\phi_{SF}(x) = \beta \left\{ \frac{\sqrt{\pi}}{2} \frac{\sqrt{2x}}{w_g} \operatorname{erf}\left(\frac{\sqrt{2x}}{w_g}\right) + \frac{1}{2} \exp\left(-\left[\frac{\sqrt{2x}}{w_g}\right]^2\right) - \frac{1}{2} \right\}, \quad (5.12)$$

where a dimensionless parameter β has been introduced, defined as

$$\beta = \frac{2\pi w_g w_{FTB}}{f\lambda}. \quad (5.13)$$

This parameter has particular significance: at high values ($\beta > 30$) the geometrical approximations hold valid, and a perfect flat-top beam may be produced with relative ease. At very low values ($\beta < 10$), the geometrical

approximations fail and the quality of the flat-top beam becomes less perfect. There is a fundamental lower limit for β at which the beam shaping problem is intractable [5.11]. A full discussion of how this parameter affects the resonator mode is beyond the scope of this paper, and is deferred to another occasion [5.13]. Since the flat-top beam is generated only at the Fourier plane of the lens, the effective phase profile of the DOE at mirror M_1 mimicking both the lens and this element is given by:

$$\phi_{DOE_1}(x) = \phi_{SF}(x) - \frac{kx^2}{2f}, \quad (5.14)$$

where the second term is the required Fourier transforming lens. In addition to an exact function for the first DOE's phase, we may use the stationary phase method to extract a closed form solution for the phase of the DOE at mirror M_2 as

$$\phi_{DOE_2}(x) = -\left[\frac{k}{2f} x^2 + \frac{1}{2} \beta \exp(-\xi^2(x)) \right], \quad (5.15a)$$

where

$$\xi(x) = \text{Inv} \left\{ \text{erf} \left(\frac{2x}{w_{FTB} \sqrt{\pi}} \right) \right\}. \quad (5.15b)$$

Here $\text{Inv}\{\cdot\}$ is the inverse function. Such a mirror will reproduce our Gaussian field at mirror M_1 , as desired. The two required mirrors to generate a flat-top beam of width $w_{FTB} = 1$ mm are shown in Fig. 5.5.

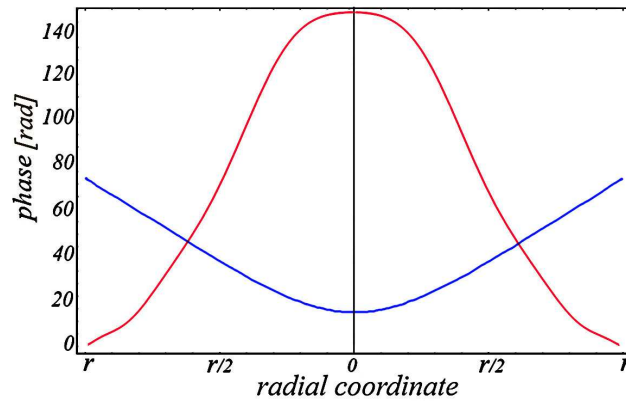


Fig. 5.5. The calculated required phases of the two DOEs, DOE_1 in blue and DOE_2 in red, to achieve the flat-top output mode.

An important aspect of the field in this resonator is its metamorphosis from a Gaussian beam at mirror M_1 , into a flat-top beam at mirror M_2 ; thus while we present the resonator concept here in terms of the generation of a flat-top beam, there are obvious advantages in exploiting the same concept for the phase-only selection of a Gaussian output mode [5.13].

5.4.2 Simulation results

The calculated beam intensities at each mirror, using $\beta \sim 21$ with $w_{FTB} = 1$ mm and $w_g = 1$ mm, are shown in Fig. 5.6 (a), together with the phase of the field at each mirror in Fig. 5.6 (b). The simulated results represented the field after stability using the Fox-Li approach, starting from random noise. In this case a Gaussian beam is produced at M_1 and a flat-top beam at M_2 . The Gaussian field (just in front of M_1) has a planar wavefront, while the flat-top beam (just in front of M_2) does not.

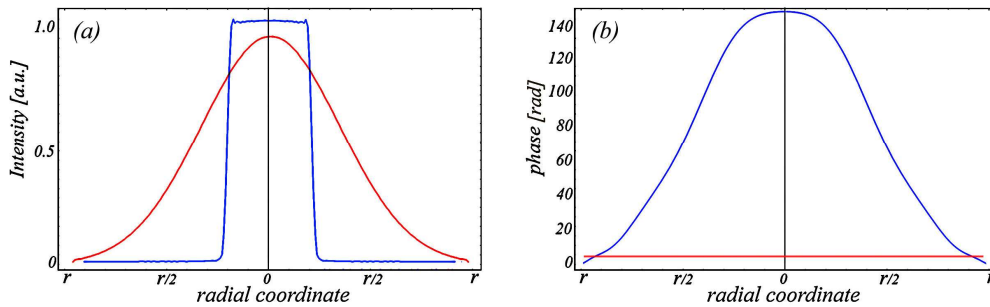


Fig. 5.6. The simulated field at mirror M_1 (red) and M_2 (blue): (a) intensity, showing a near perfect flat-top beam at M_2 , changing into a perfect Gaussian after propagating across the resonator to M_1 , (b) phase of the field, with a flat wavefront at M_1 as anticipated from the design.

A cross-section through the resonator of the stabilised field is shown in Fig. 5.7, together with density plots of the field intensity at various planes in the resonator.

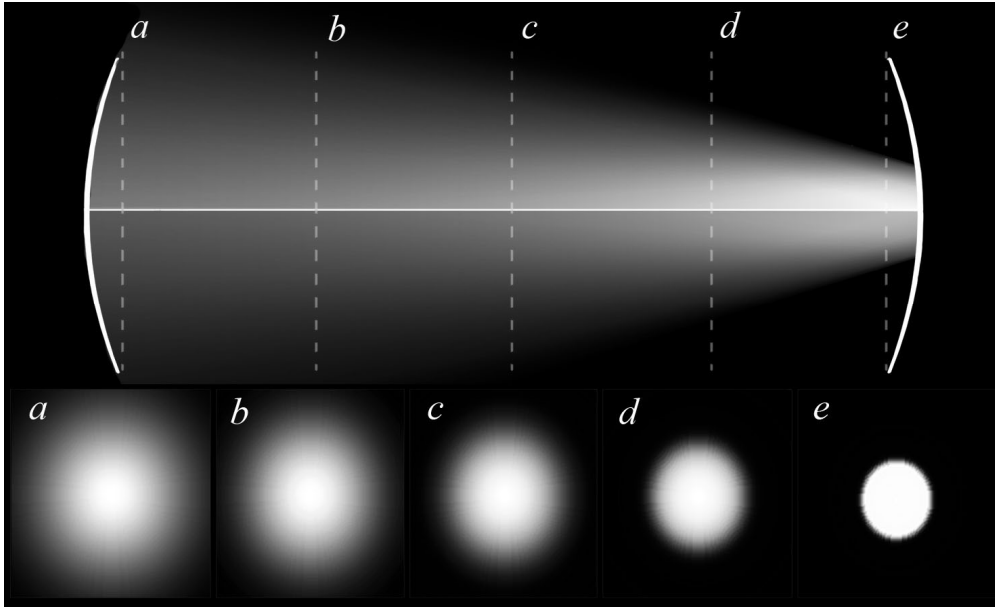


Fig. 5.7. The simulated field as it propagates across the resonator after stabilization, from M_1 (left) to M_2 (right). The perfect Gaussian beam (a) gradually changes into a perfect flat-top beam (e) on one pass through the resonator. In this design the field also decreases in size, as noted from the size of the grey scale images.

Because of the transformation during propagation from a Gaussian to a flat-top beam, the region of constant intensity is limited to near mirror M_2 . This impacts on energy that may be extracted from such a resonator since the gain volume would be somewhere between a single mode Gaussian and a single mode flat-top beam. The phase of the field at M_2 requires that a suitable DOE external to the cavity be used to convert the phase of the flat-top beam into a planar wavefront, should this be required.

5.5 Discussion

It is pertinent at this point to draw comparisons between the two approaches outlined. The first difference lies in the dynamics of the round trip losses, as shown in Figs. 5.8 (a) and (b). Clearly the losses are higher after mode stabilization in our approach (henceforth labelled *A*) as compared to the Belanger and Pare approach (henceforth labelled *B*), but this in turn results in faster convergence to the fundamental mode of this resonator. In our resonator concept (*A*) the mode stabilizes in less than half the number of round trips required for stabilization in the comparative conjugating resonator (*B*). The

higher losses of resonator *A* may be explained by the fact that the Gaussian field on mirror M_1 in design *A* has necessarily higher losses than is the case of a near flat-top beam on the same mirror in design *B*.

It is evident in both resonators that the losses per round trip oscillate prior to stabilizing. This has been noted previously in other resonator types, and explained in terms of the stability parameters of the resonator [5.14]. The oscillating modes corresponding to the loss oscillations are shown in Fig. 5.8 as insets. Here the field changes from a concave flat-top, through a perfect flat-top, to a convex flat-top.

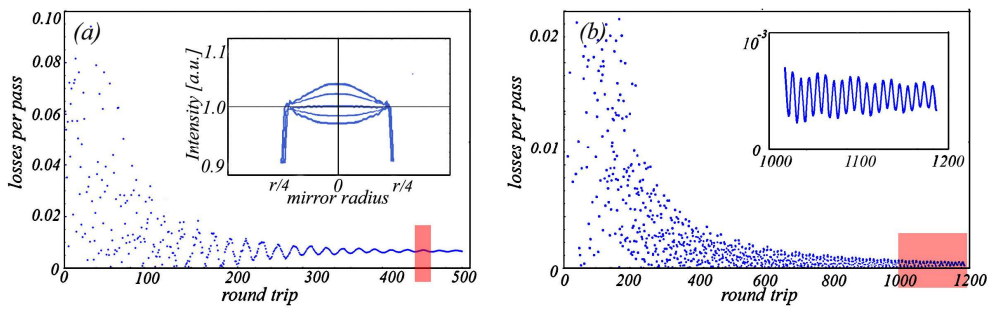


Fig. 5.8. The simulated losses as a starting field of random noise is propagated through the resonator, shown as a function of the number of round trips taken, for: (a) resonator *A* and (b) resonator *B*. The losses stabilize in both resonators, and both show a characteristic oscillation in the losses as the field converges to the stable mode of lowest loss.

Both resonators generate the same size flat-top beam at the output coupler end, but resonator *B* by its nature maintains almost the same field profile throughout its length. This would not be the case if the optical path length was much greater than the Rayleigh length of the field, but then it has already been pointed out that this resonator concept does not work at such distance as all modes have nearly spherical wavefronts, making mode discrimination weak [5.3]. In contrast, by design our resonator (*A*) changes the mode very rapidly from one mirror to the other, and thus does not suffer from this drawback. The price to pay is in the mode volume: resonator *A* has a larger mode volume, and potentially would be able to extract more energy from the gain region. Furthermore, in the case of resonator *B*, if the gain medium is to be placed such that only a flat-top beam passes through it, then it must be restricted in size and placed near the output coupler.

Both designs have restrictions on the size and quality of flat-top beam that may be generated. While in theory the design method for resonator *B* would allow any size and quality FGB to be generated, if the Rayleigh range is not large compared to the resonator length, and the Fresnel number of the resonator is not large enough, then losses will increase and the quality of the flat-top profile will deteriorate in a concomitant manner. There is thus a lower limit for the Rayleigh range to ensure a quality flat-top beam. Resonator *A* is restricted to beam sizes such that β is large ($\beta \geq 30$), since for small β the quality of the flat-top becomes poor, with large skirt regions and rounded central regions, while below a threshold value (typically $\beta < 4$) the method breaks down completely and can no longer be applied. Thus again there is a lower limit, this time for β , so ensure a quality flat-top beam. In addition, the Fresnel number of the resonator in both options must be suitably large in order to avoid diffractive losses and associated profile distortions, and thus this too places a limit on what may be achieved. Thus one must be judicious in the choice of the dimensions of the resonator in relation to the desired fields. For example, an $N = 100$ field will ensure an excellent flat-top beam, but this will require a short resonator length and/or large mirrors in order to ensure both the Rayleigh range of the field and the Fresnel number of the resonator are both suitably large.

A final point of departure is the cost and complexity of implementing the resonator concepts. Resonator *B* requires only one DOE, and creates a planar wavefront top-hat-like beam at the planar output coupler side. In contrast, resonator *A* has DOEs at both ends of the resonator, and does not produce a planar wavefront at the flat-top beam end. Thus at least one additional DOE is required external to the cavity to create the same field in phase as in resonator *B*. However the major advantage of resonator *A* is the ability to generate a planar wavefront Gaussian field as an output by low loss phase-only mode selection.

We end by indicating how the phase profiles defined here may be implemented in practice. If the desired phase of the DOE is given by ϕ_{DOE} , then this may either be implemented as an etched height structure in a transmission element (of refractive index n), or a reflective mirror, with associated surface

feature profiles given by $h = \frac{\lambda\phi_{DOE}}{2\pi(n-1)}$ and $h = \frac{\lambda\phi_{DOE}}{2\pi}$ respectively.

5.5 Conclusion

We have presented two methods of creating flat-top beams as the output mode of a laser resonator where both approaches lead to analytical expressions for the required mirror surfaces. The first approach was to use an approximation to flat-top beams and apply phase conjugating mirrors at either end of the resonator. We showed that this leads to simple expressions for the mirror surfaces. In the second approach a suitable diffractive optical element converts a Gaussian beam into a flat-top beam at the Fourier plane of a lens. This method shows fast convergence and relatively low round trip loss for the fundamental mode of the resonator.

Chapter 6

Gaussian mode selection with intra-cavity diffractive optics

In this Chapter we outline a resonator design that allows for the selection of a Gaussian mode by diffractive optical elements (phase only intra-cavity beam shaping). This is made possible by the metamorphosis of a Gaussian beam into a flat-top beam during propagation from one end of the resonator to the other. By placing the gain medium at the flat-top beam end, it is possible to extract high energy in a low-loss cavity. A further feature of this resonator is the ability to select the field properties at either end of the cavity almost independently, thus opening the way to minimize the output divergence while simultaneously maximizing the output energy.

6.1 Introduction

Traditionally laser beams are generated in Fabry-Perot type resonators, where the mirror surfaces are spherical. When the resonator is chosen to be stable, a low-loss fundamental mode may be forced to oscillate by suitable choice of internal aperture. However, the power loss discrimination between the low order modes is often poor, and the small beam waist results in poor power extraction. Conversely, if an unstable configuration is employed, the mode volume is large and mode discrimination good, but this is at the expense of high intrinsic loss for the oscillating modes, making such cavities suitable only for lasers with high gain. A major advance to overcome such problems was the introduction of so-called graded-phase mirrors [5.2, 5.3]. It was shown that a resonator with grade-phase mirrors could discriminate against undesired modes by altering the generalized radius of curvature of the incoming beam according to [5.2]:

$$\frac{1}{R_2} = \frac{1}{R_1} - \frac{\int_{-\infty}^{\infty} x \left(\frac{d\phi_M}{dx} \right) \psi_1^2(x) dx}{\int_{-\infty}^{\infty} x^2 \psi_1^2(x) dx}, \quad (6.1)$$

where R_1 and R_2 are the generalized radii of curvature just prior and just after the graded-phase mirror (ϕ_M) respectively. Eq. (6.1) indicates that the real radius of curvature of the beam is changed by the phase function of the graded-phase mirror, and moreover, this change is dependent on the incoming amplitude of the field, $\psi_1(x)$. In other words, it is possible for such a graded-phase mirror to discriminate against modes that do not have the proper distribution, $\psi_1(x)$. However, when the graded-phase mirror is spherical (assuming the paraxial limit), the change in curvature of the beam becomes independent of the incoming amplitude of the field, $\psi_1(x)$, since the derivative in the integrand becomes proportional to x . Unfortunately, for Gaussian beams the required graded-phase mirror surface is spherical, therefore annulling the aforementioned discrimination process. To put this another way, the graded-phase mirror approach cannot be used to select between any of the Hermite-Gaussian (in resonators with rectangular symmetry) or Laguerre-Gaussian (in resonators with circular symmetry) modes, and therefore by definition not the lowest order Gaussian mode either. The reason is simply that under free space propagation all such fields have an identical real radius of curvature, defined by spherical wavefronts, and thus reverse propagating such beams to find the appropriate conjugate always returns a solution that requires a spherical curvature mirror. Note that the form of the graded-phase mirror here might in fact be a deformable mirror, a diffractive mirror, or approximated by a transmission diffractive optical element or even an intra-cavity phase-only spatial light modulator. The limitation is not in how the phase element is implemented, but rather by the fundamental physics governing the propagation of Gaussian beams.

6.2 Gaussian mode selection

It is possible to overcome this problem by metamorphosing a Gaussian beam into another desired shape. Since the resulting propagation will not follow that of a Gaussian beam in free space, the resulting beam after propagation may be discriminated against in the usual manner. In this Section we propose a resonator concept that produces a Gaussian mode using diffractive optical elements by intra-cavity metamorphosis of a Gaussian beam at the output coupler end, to a flat-top beam at the opposite end of the cavity. It is well known that flat-top beams have been favored over Gaussian beams in those applications where high power extract is required [5.5]. This is because flat-top beams cover a larger mode volume for the same Gaussian beam size, and they overcome the poor saturation and energy extraction at the edge of Gaussian beams. Such a resonator has the possibility of low diffraction loss, and high energy extraction, while producing a low divergence Gaussian beam.

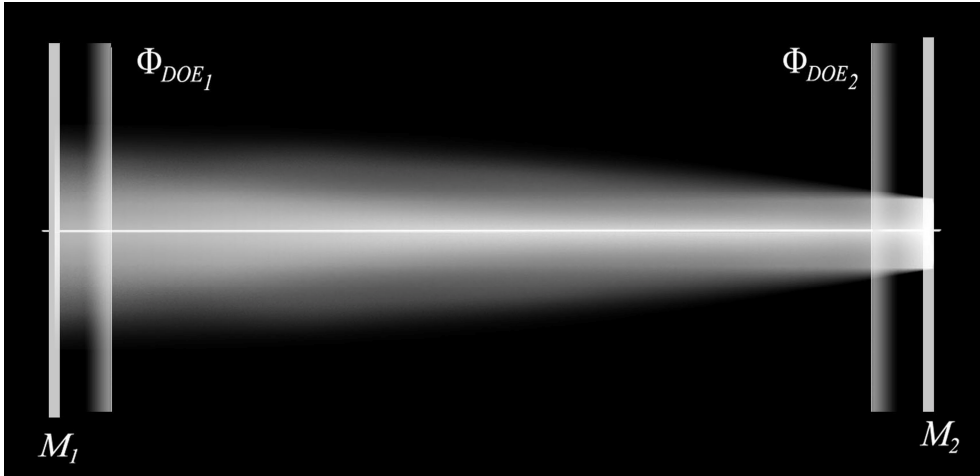


Fig. 6.1: Schematic of the resonator concept. M_1 and M_2 are flat mirrors, Φ_{DOE_1} and Φ_{DOE_2} are the effective phase profiles of the DOE₁ at mirror M_1 and DOE₂ at mirror M_2 correspondingly.

We illustrate the concept graphically in Fig. 6.1: a flat-flat resonator is modified with suitable intra-cavity diffractive optical elements, where the sum of the flat mirror and adjacent transmission DOE mimics a graded-phase mirror. Our task is to outline the functional form of the two DOEs. To do this, we consider a circular Gaussian field at mirror M_1 of the form $u_1(\rho) = \exp[-(\rho/w_0)^2]$, where w_0 is the radius where the field is at $1/e$ of its peak value. If the DOE at mirror M_1 is made up of a Fourier transforming lens and a phase only

transmission element, ϕ_{SF} , and the resonator length is selected to match the focal length of the Fourier transforming lens ($L = f$), then the resulting field at mirror M_2 will be given by:

$$u_2(r) = -i \frac{k}{f} \exp(ikf) \exp\left(\frac{ikr^2}{2f}\right) \int_0^\infty u_1(\rho) \exp[i\phi_{SF}(\rho)] J_0\left(\frac{kr\rho}{f}\right) \rho d\rho. \quad (6.2)$$

We may apply the method of stationary phase to find an analytical solution for the phase function ϕ_{SF} , such that the field u_2 is a perfect flat-top beam, of width w_{FTB} [5.11]:

$$\phi_{SF}(\rho) = \beta \frac{\sqrt{\pi}}{2} \int_0^{\frac{\rho}{w_0}} \sqrt{1 - \exp(-\xi^2)} d\xi, \quad (6.3)$$

where a dimensionless parameter β has been introduced, defined as

$$\beta = \frac{2\pi w_0 w_{FTB}}{f\lambda}. \quad (6.4)$$

Since the flat-top beam is generated only at the Fourier plane of the lens, the effective phase profile of the DOE at mirror M_1 mimicking both the lens and this element is given by:

$$\phi_{DOE_1}(\rho) = \phi_{SF}(\rho) - \frac{k\rho^2}{2f}, \quad (6.5)$$

where the second term is the required Fourier transforming lens. In addition to an exact function for the first DOE's phase, we state here (the proof is beyond the scope of this discussion and will be published elsewhere) that it is also possible to use the stationary phase method to extract a closed form solution for the phase of the DOE at mirror M_2 as:

$$\phi_{DOE_2}(r) = \arg \left\{ \exp \left[i \left(\frac{k}{2f} r^2 + \phi_{SF}(\rho(r)) - \frac{\beta r \rho(r)}{w_{FTB} w_0} \right) \right] \right\}, \quad (6.6a)$$

where from the stationary phase condition $r/w_{FTB} = \partial\phi_{SF}/\partial\rho$ we may find the unknown function:

$$\rho(r) = w_0 \sqrt{-\ln \left[1 - \left(\frac{2r}{\sqrt{\pi} w_{FTB}} \right)^2 \right]}, \quad (6.6b)$$

Such a mirror will reproduce our Gaussian field with a flat wavefront at mirror M_1 , as desired. Moreover, since the field at mirror M_2 is a flat-top beam, there exists the possibility for uniform gain saturation and high energy extraction if the gain medium is placed at this end of the resonator cavity.

6.3 Numerical analysis and discussion

It is instructive to consider the flat-top beam as a Flattened Gaussian Beam (FGB) of order N [5.9]. The advantage of this profile over others is that it offers a simple analytical expression for the beam profile at any propagation distance z , and furthermore, the Gaussian and flat-top profiles are returned when $N = 1$ and $N \rightarrow \infty$ respectively. It is well known that flat-top beams are able to fill a larger mode volume without the adverse affects of diffraction for similar sized Gaussian beams, due to the fast drop in intensity at the edges of the beam. In fact, it has been pointed out [5.16] that even a relatively low order FGB fills nearly four times more volume of a laser rod of diameter $d = 3w_0$ than a Gaussian beam could, due to the smaller Gaussian field required in order to avoid hard edge clipping. In addition, the peak intensity of the FGB is smaller than that of a Gaussian beam of the same width and energy, reaching a minimum of only half the peak intensity when the order $N \gg 1$. This is important when considering practical issues such as thermally induced stress fracture, and thermal aberrations, in solid state gain materials. However, the disadvantage of such beams is the larger beam quality factor, and hence shorter Rayleigh range, thus reducing the useful length of the gain medium that will experience the uniform beam. The Rayleigh range of such a beam is given by z_R/N where z_R is the Rayleigh range of a Gaussian beam with the same parameters [5.10]. Clearly the price to be paid for a perfect flat-top beam ($N > 100$) is a significantly reduced Rayleigh range. These results are important in understanding the depth of field of the flat-top beam for gain extraction purposes.

In our design these points may be balanced through the use of Eq. 6.5; herein lie the salient parameters of the desired Gaussian beam size, the desired

flat-top beam size, and the degree of flatness of the beam itself, β , which is proportional to the order of the FGB. If all three are to be chosen independently for a particular wavelength, then the focal length of the Fourier transforming lens, and hence the length of the resonator, must be appropriately selected using Eq. (6.5), while the phase functions of the DOEs maintain the same functional form, i.e., only the dimensionless parameter β changes in the equations. The ease with which the DOEs may be calculated for various parameters of the desired mode is a unique feature of this resonator design. Essentially the propagation of the Gaussian beam outside the resonator may be determined almost independently of the flat-top mode inside the gain volume. There are obvious advantages to such a flexible design.

To expound on the concept, we consider the example of a resonator designed to produce a Gaussian beam with a width of $w_0 = 1$ mm, from which we deduced the required Gaussian beam half angle divergence of $\theta = \lambda/\pi w_0 = 0.34$ mrad ($\lambda = 1064$ nm). With this fixed, we may now select any two of the remaining three parameters: resonator length, flat-top beam size, or degree of flatness of our flat-top beam (β). If our gain medium is a rod of radius 3 mm and length 100 mm, then we may wish to select a flat-top beam of $w_{FTB} = 2$ mm, while $\beta = 23$ will ensure a high fidelity flat-top beam that propagates throughout the gain length without significant changes of intensity profile. From Eq. (6.5) we then deduce that the required resonator length ($L = f$) is given by ~ 500 mm. Fig. 6.2 shows the results of a numerical simulation of the aforementioned resonator, starting with a field of random noise and propagated following the Fox-Li approach [2.2] until stability, with mirror radii of $4w_0$. Fig. 6.2(a) shows the stable fields at either end of the resonator – the expected Gaussian and flat-top beams as per the design. Fig. 6.2(b) shows the numerically determined phase of each DOE. Near the beam edge there is a slight discrepancy between the analytically calculated phase of the second DOE and the numerically determined phase; this is due to the use of the stationary phase approximation in the analytical equations. The same design procedure may be adopted to accommodate other constraints, for example, the length of the resonator or the complexity of the DOEs themselves.

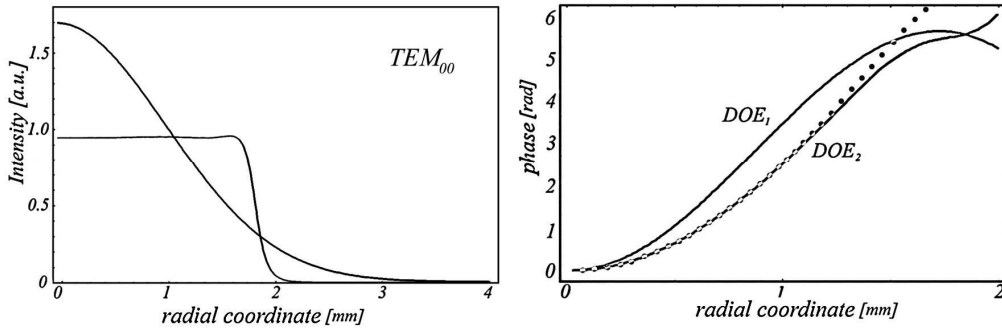


Fig. 6.2: Numerical results of the Fox–Li analysis, showing (a) Gaussian and flat-top beams after starting from random noise, and (b) calculated phase profile of each DOE, with the analytical phase function for the second DOE shown as data points.

It is also instructive to extend the example above to consider the mode discrimination of this resonator. Without any gain considerations, the fundamental Gaussian/flat-top mode has the lowest loss (0.34%) with the next lowest loss modes shown in Fig. 6.3. These three modes have higher losses, by factors of 1.06 (TEM_{10}), 1.18 (TEM_{01}) and 1.47 (TEM_{11}) respectively, but also have significantly smaller mode volumes within the gain region, decreased relative to the fundamental mode by a factor of 0.65 (TEM_{10}), 0.29 (TEM_{01}) and 0.33 (TEM_{11}) respectively. Thus when gain is included (at the flat-top end), the significantly increased volume for our Gaussian/flat-top mode should aid mode discrimination, whereas in conventional resonator designs it is often the reverse: the Gaussian mode would have a lower mode volume than other competing modes. In a practical system the discrimination could be further enhanced by the inclusion of suitable apertures on the Gaussian end of the resonator.

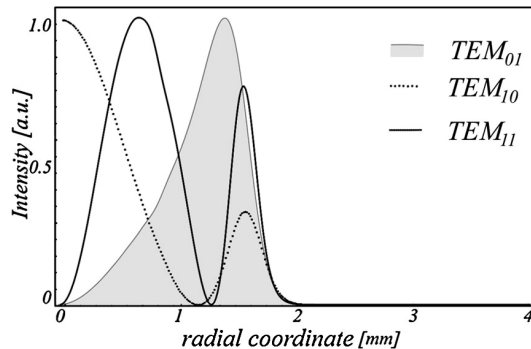


Fig. 6.3: Cross-sections of the first three higher-order competing modes, shown at mirror M_2 .

6.4 Conclusion

In conclusion, we have shown that it is possible to design a resonator for a Gaussian beam output but with the advantage of a flat-top beam in the gain region. The metamorphosis from one beam shape to another is achieved through phase-only optical elements. Such a configuration lends itself to high energy extraction with good competing mode discrimination in a low divergence output mode.

Conclusion

In this thesis we have presented new methods for intra-cavity beam shaping. To illustrate the methods we have provided both an analytical and numerical analysis of novel resonator systems which are able to produce customised phase and intensity distributions.

Naturally, intra-cavity beam shaping can not be phase or amplitude only due to the limited radius and the defined curvature of the mirrors. Both these parameters have the influence on the final output beam profile. That is why it is difficult to divide the systems where we have used phase or amplitude beam transformations in the cavity only. In this thesis we have assumed that the division between phase and amplitude intra-cavity beam shaping is connected to a comparison of the geometry of our system with conventional resonators, including parabolic mirrors and a ring aperture on both mirrors.

In Chapter 2 we have outlined a new approach (matrix method), which is based on the Fox-Li algorithm and can decrease the computation time of both the Fox-Li algorithm and any integral iteration algorithms. The method can be used for any class of integral iteration algorithms which has the same calculation integrals, with changing integrands (where the integrand is the field of the light wave in the case of the Fox-Li algorithm, IFTA, and screen method). The given method appreciably decreases the computation time of these algorithms and approaches that of a single iteration.

In Chapter 3 a new approach to modeling the spatial intensity profile from Porro prism resonators was proposed based on rotating loss screens to mimic the apex losses of the prisms. A numerical model based on this approach was presented which correctly predicted the output transverse field distribution found experimentally from such resonators. This work has implications on how such resonators are used in the field. Variable output coupling based on rotating the prisms is often employed, but as has been shown in Chapter 3, this will have a significant impact on the output mode from the laser, affecting laser beam propagation, far field laser intensity and laser brightness.

In Chapter 4 we have presented a new approach of generating Bessel–Gauss beam as the output namely the deployment of a suitable amplitude filter at the Fourier plane of a conventional resonator configuration with only spherical curvature optical elements. As we can see, the approach is combination of both amplitude and phase shaping inside a cavity. We also wish to point out some practical implications in generating of Bessel–Gauss beams from such a resonator. Firstly, since the resonator consists of only conventional optical elements (spherical curvature mirrors and circular apertures) no special alignment techniques are required. Secondly, due to the fact that the order of the Bessel–Gauss beams of lowest loss is determined only by the diameter of mirror M_2 (see Fig. 4.1), a simple variable aperture (iris) at the position of mirror M_2 should suffice as a mode selector in much the same way that the various Hermite–Gauss modes may be selected by suitable aperture choice.

In Chapter 5 we have presented the analytical and numerical analyses of two new resonator systems for generating flat–top–like beams. Both approaches lead to closed form expressions for the required cavity optics, but differ substantially in the design technique, with the first based on reverse propagation of a flattened Gaussian beam, and the second a metamorphosis of a Gaussian into a flat–top beam. We showed that both have good convergence properties, and result in the desired stable mode. The first approach was to use an approximation to flat–top beams and apply phase conjugating mirrors at either end of the resonator. We showed that this leads to simple expressions for the mirror surfaces. In the second approach a suitable diffractive optical element converts a Gaussian beam into a flat–top beam at the Fourier plane of a lens. This method shows fast convergence and relatively low round trip loss for the fundamental mode of the resonator.

In Chapter 6 we have outlined a resonator design that allows for the selection of a Gaussian mode by diffractive optical elements. This is made possible by the metamorphosis of a Gaussian beam into a flat–top beam during propagation from one end of the resonator to the other. By placing the gain medium at the flat–top beam end, it is possible to extract high energy in a low–loss cavity.

References

- [1.1] J. D. Jackson, "Classical Electrodynamics," 3rd ed., John Wiley & Sons, Inc., 1998
- [1.2] P. W. Milonni and J. H. Eberly, "Lasers," John Wiley & Sons, Inc., 1988
- [1.3] N.V. Karlov, "Quantum electronics lectures," 2nd ed., Science, Moscow, 1988
- [2.1] A. E. Siegman, "Laser beams and resonators: The 1960s," *IEEE J. Select. Topics Quant. Electron.* 6, 1380-1388, 2000.
- [2.2] A. G. Fox and T. Li, "Resonant modes in a maser interferometer," *Bell Syst. Tech. J.* 40, 453-488, 1961.
- [2.3] G. Korn, T. Korm, Mathematics handbook, Science, Moscow, 1970.
- [2.4] S. A. Collins, "Lens-system diffraction integral written terms of matrix optics," *J. Opt. Soc. Am. A* 60, 1168-1177, 1970.
- [2.5] Takayuki Hirai, Keiji Fuse, Kenichi Kurisu and Keiji Ebata, "Development of Diffractive Beam Homogenizer," *SEI Technical Review*, 60, 17-23, 2005.
- [2.6] R. J. Noll, "Zernike polynomials and atmospheric turbulence," *J. Opt. Soc. Am.* 63 (3), 207-211, 1976.
- [2.7] J. W. Goodman, Introduction to Fourier Optics, McGraw-Hill Book, New York, 1968.
- [3.1] G. Gould, S. Jacobs, P. Rabinowitz and T. Shultz, "Crossed Roof Prism Interferometer," *Appl. Opt.* 1, 533-534, 1962.
- [3.2] I. Kuo and T. Ko, "Laser resonators of a mirror and corner cube reflector: analysis by the imaging method," *Appl. Opt.* 23, 53-56, 1984.
- [3.3] G. Zhou and L.W. Casperson, "Modes of a laser resonator with a retroreflecting roof mirror," *Appl. Opt.* 20, 3542-3546, 1981.
- [3.4] J. Lee and C. Leung, "Beam pointing direction changes in a misaligned Porro prism resonator," *Appl. Opt.* 27, 2701-2707, 1981.
- [3.5] Y.A. Anan'ev, V.I. Kuprenyuk, V.V. Sergeev and V.E. Sherstobitov, "Investigation of the properties of an unstable resonator using a dihedral corner reflector in a continuous-flow cw CO₂ laser," *Sov. J. Quantum Electron.* 7, 822-824, 1977.
- [3.6] I. Singh, A. Kumar and O.P. Nijhawan, "Design of a high-power Nd:YAG Q-switched laser cavity," *Appl. Opt.* 34, 3349-3351, 1995.
- [3.7] N. Hodgson and H. Weber, "Laser Resonators and Beam Propagation," (Springer, 2005), Chap. 17.

- [3.8] Y.Z. Virnik, V.B. Gerasimov, A.L. Sivakov and Y.M. Treivish, "Formation of fields in resonators with a composite mirror consisting of inverting elements," *Sov. J. Quantum Electron.* 17, 1040–1043, 1987.
- [3.9] T.A. Anan'ev, "Unstable prism resonators," 3, 58–59, 1973.
- [3.10] A. E. Siegman, H. Y. Miller, "Unstable Optical Resonator Loss Calculations Using Prony Method," *Appl. Opt.* 9, 2729–2736, 1970.
- [3.11] I. A. Litvin, L. Burger, A. Forbes, "Petal-like modes in Porro prism resonators," *Opt. Express.*, 15, 14065-14077, 2007.
- [4.1] J. Durnin, "Exact solutions for nondiffracting beams. I. The scalar theory," *J. Opt. Soc. Am. A* 4, 651–654, 1987.
- [4.2] J. Durnin, J.J. Miceli, J.H. Eberly, "Diffraction-free beams," *Phys. Rev. Lett.* 58, 1499–1501, 1987.
- [4.3] J. Durnin, J.H. Eberly, "Diffraction free arrangement," *patent no. 4887885*, December 19, 1989.
- [4.4] D. McGloin, K. Dholakia, "Bessel beams: diffraction in a new light," *Contemporary Physics* 46, 15–28, 2005.
- [4.5] I.A. Litvin, M. G. McLaren, A. Forbes, "A conical wave approach to calculating Bessel–Gauss beam reconstruction after complex obstacles," *Opt. Commun.*, 282 (6), 1078-1082, 2008.
- [4.6] J.K. Jabzynski, "A diffraction-free resonator," *Opt. Commun.* 77, 292–294, 1990.
- [4.7] J. Rogel–Salazar, G.H.C. New, S. Chavez–Cerda, "Bessel-Gauss beam optical resonator," *Opt. Commun.* 190, 117–122, 2001.
- [4.8] A.N. Khilo, E.G. Katranji, A.A. Ryzhevich, "Axicon-based. Bessel resonator: Analytical description and experiment," *J. Opt. Soc. Am. A* 18, 1986–1992, 2001.
- [4.9] C.L. Tsangaris, G.H.C. New, J. Rogel–Salazar, "Unstable Bessel beam resonator," *Opt. Commun.* 223, 233–238, 2003.
- [4.10] P. Paakkonen, J. Turunen, "Resonators with BesselGauss modes," *Opt. Commun.* 156, 359–366, 1998.
- [4.11] J.C. Gutierrez–Vega, R. Rodríguez–Masegosa, S. Chavez–Cerda, "Bessel–Gauss resonator with spherical output mirror: geometrical- and wave-optics analysis," *J. Opt. Soc. Am. A* 20, 2113–2122, 2003.
- [4.12] R.I. Hernandez–Aranda, S. Chavez–Cerda, J. C. Gutierrez–Vega, "Theory of the unstable Bessel resonator," *J. Opt. Soc. Am. A* 22, 1909–1917, 2005.
- [4.13] A.Hakola et al, "Bessel–Gauss output beam from a diode – pumped Nd:YAG laser," *Opt. Commun.*, 238 (4-6), 335-340, 2004.
- [4.14] I. A. Litvin and A. Forbes, "Bessel–Gauss Resonator with Internal Amplitude Filter," *Opt. Commun.*, 281 (9), 2385-2392, 2008.

- [5.1] Laser Beam Shaping, Theory and Techniques, ed Dickey/Holswade. (*New York: Marcel Dekker, Inc.*), 2000.
- [5.2] P.A. Belanger P.A., C. Pare, "Optical resonators using graded-phase mirrors," *Opt. Lett.* 16, 1057–1059, 1991.
- [5.3] C. Pare, P.A. Belanger, "Custom Laser Resonators Using Graded-Phase Mirror," *IEEE J. of Quantum Electron.* 28, 355–362, 1992.
- [5.4] P. A. Belanger, R. L. Lachance, C. Pare, "Super-Gaussian output from a CO₂ laser by using a graded-phase mirror resonator," *Opt. Lett.* 17, 739–741, 1992.
- [5.5] J. R. Leger, D. Chen, Z. Wang, "Diffractive optical element for mode shaping of a Nd:YAG laser," *Opt. Lett.* 19, 108–110, 1994.
- [5.6] J. R. Leger, D. Chen, K. Dai, "High modal discrimination in a Nd:YAG laser resonator with internal phase gratings," *Opt. Lett.* 19, 1976–1978, 1994.
- [5.7] D. L. Shealy, J.A. Hoffnagle, "Laser beam shaping profiles and propagation," *Appl. Opt.* 45, 5118–5131, 2006.
- [5.8] Forbes A., Strydom H.J., Botha L.R., and Ronander E., "Beam delivery for stable isotope separation," *Proc. SPIE* 4770, 13–27, 2002.
- [5.9] F. Gori, "Flattened Gaussian beams," *Opt. Commun.* 107, 335–341, 1994.
- [5.10] B. Lu, S. Luo, "General propagation equation of flattened Gaussian beams," *J. Opt. Soc. Am. A* 17, 2001–2004, 2000.
- [5.11] L. A. Romero, F. M. Dickey, "Lossless laser beam shaping," *J. Opt. Soc. Am. A* 13, 751–760, 1996.
- [5.12] F. M. Dickey, S. C. Holswade, "Gaussian laser beam profile shaping," *Opt. Eng.* 35, 3285–3295, 1996.
- [5.13] I. A. Litvin and A. Forbes, "Gaussian mode selection with intra-cavity diffractive optics," *Opt. Lett.*, 34, 2991-2993, 2009.
- [5.14] L. Burger, A. Forbes, "Kaleidoscope modes in large aperture Porro prism resonators," *Opt. Express* 16, 12707–12714, 2008.
- [5.15] I. A. Litvin and A. Forbes, "Intra-cavity flat-top beam generation," *Opt. Express*, 17 (18), 15891-15903, 2009.
- [5.16] A. E. Siegman, *Lasers (University Science Books, 1986)*.
- [5.17] I. A. Litvin, N. Khilo, A. Forbes, V. Belyi, "Intra-cavity generation of longitudinally dependant Bessel like beams," accepted for publication in *Opt. Express*, 2010.